

**Beyond modelocking: High repetition-rate frequency  
combs derived from a continuous-wave laser**

by

**Daniel C. Cole**

B.S., Washington University in St. Louis, 2012

M.S., University of Colorado, 2015

A thesis submitted to the  
Faculty of the Graduate School of the  
University of Colorado in partial fulfillment  
of the requirements for the degree of  
Doctor of Philosophy  
Department of Physics  
2018

This thesis entitled:  
Beyond modelocking: High repetition-rate frequency combs derived from a continuous-wave laser  
written by Daniel C. Cole  
has been approved for the Department of Physics

---

Scott A. Diddams

---

Reader Two

Date \_\_\_\_\_

The final copy of this thesis has been examined by the signatories, and we find that both the content and the form meet acceptable presentation standards of scholarly work in the above mentioned discipline.

Cole, Daniel C. (Ph.D., Physics)

Beyond modelocking: High repetition-rate frequency combs derived from a continuous-wave laser

Thesis directed by Dr. Scott A. Diddams

Optical frequency combs based on modelocked lasers have revolutionized precision metrology by facilitating measurements of optical frequencies, with implications both for fundamental scientific questions and for applications such as fast, broadband spectroscopy. In this thesis, I describe advances in the generation of frequency combs without modelocking in platforms with smaller footprints and higher repetition rates, with the ultimate goal of bringing frequency combs to new applications in a chip-integrated package. I discuss two approaches for comb generation: parametric frequency conversion in Kerr microresonators and active electro-optic modulation of a continuous-wave laser. After introducing microresonator-based frequency combs (microcombs), I discuss two specific developments in microcomb technology: First, I describe a new, extremely reliable method for generation of soliton pulses through the use of a phase-modulated pump laser. This technique eliminates the dependence on initial conditions that was formerly a universal feature of these experiments, presenting a solution to a significant technical barrier to the practical application of microcombs. Second, I present observations of *soliton crystal* states with highly structured ‘fingerprint’ optical spectra that correspond to ordered pulse trains exhibiting crystallographic defects. These pulse trains arise through interaction of solitons with avoided mode-crossings in the resonator spectrum. I also discuss generation of Kerr soliton combs in the Fabry-Perot (FP) geometry, with a focus on the differences between the FP geometry and the ring geometry that has been the choice of most experimenters to date. Next, I discuss combs based on electro-optic modulation. I introduce the operational principle, and then describe the first self-referencing of a frequency comb of this kind and a proof-of-principle application experiment. Finally, I discuss a technique for reducing the repetition rate of a high repetition-rate frequency comb, which will be a necessary post-processing step for some applications.

## Contents

<b>1</b>	Introduction to microresonator-based frequency combs	<b>1</b>
1.1	Optical microring resonators . . . . .	1
1.1.1	Resonant enhancement in a microring resonator . . . . .	3
1.1.2	Thermal effects in microresonators . . . . .	4
1.2	Microring resonator Kerr frequency combs . . . . .	6
1.2.1	A model for Kerr-comb nonlinear optics: The Lugiato-Lefever equation . . . . .	7
1.3	Description of Kerr-comb outputs using the Lugiato-Lefever equation . . . . .	9
1.3.1	Analytical investigation of the resonator's CW response . . . . .	9
1.3.2	Kerr comb outputs: extended modulation-instability patterns . . . . .	11
1.3.3	Kerr comb outputs: solitons . . . . .	12
<b>2</b>	Theory of Kerr frequency combs in Fabry-Perot resonators	<b>18</b>
2.1	General relationship between the ring LLE and the FP-LLE . . . . .	20
2.2	Extended patterns in the FP-LLE . . . . .	20
2.3	Solitons in the FP-LLE . . . . .	21
2.3.1	Analytical approximation for solitons in the FP-LLE . . . . .	21
2.3.2	Existence range of single solitons . . . . .	22
2.3.3	Generation of single solitons through laser frequency scans . . . . .	24
<b>3</b>	Microresonator-based frequency combs: Summary and outlook	<b>26</b>

<b>4 EOM Combs</b>	<b>28</b>
4.1 Principle of operation . . . . .	28
4.2 Generation of an EOM comb and detection of its carrier-envelope offset frequency .	30
4.3 Noise considerations in EOM comb generation . . . . .	33
4.4 Application: Optical frequency division via double pinning . . . . .	35
4.5 Outlook . . . . .	37
<b>References</b>	<b>38</b>

## Figures

1.1	Optical microdisk resonator . . . . .	2
1.2	Thermal bistability in microresonators . . . . .	5
1.3	An illustration of four-wave mixing and frequency-comb generation. . . . .	6
1.4	Solution space for the Lugiato-Lefever equation . . . . .	9
1.5	Investigation of the circulating CW power in a Kerr resonator . . . . .	11
1.6	Extended-pattern solutions to the LLE . . . . .	13
1.7	Soliton solutions to the LLE . . . . .	14
1.8	Kerr-soliton energy-level diagram . . . . .	16
2.1	Relationship between the physical field in the Fabry-Perot cavity and the co-moving field $\psi$ . . . . .	19
2.3	Boundaries of soliton existence in the FP-LLE . . . . .	23
2.4	Transition from extended patterns to single solitons in the FP-LLE . . . . .	24
4.1	Operating principle of an electro-optic modulation comb . . . . .	29
4.2	Experimental setup for detection of the carrier-envelope offset frequency of an EOM comb after generation of a coherent supercontinuum . . . . .	31
4.3	Spectral broadening for generation of an octave-spanning supercontinuum . . . . .	32
4.4	Self-referencing of an EOM comb . . . . .	33
4.5	Investigation of the noise properties of the EOM comb . . . . .	34
4.6	Photodetected carrier-envelope-offset frequency signal with different sources for $f_{rep}$ . . . . .	35
4.7	Stable microwave generation with an EOM comb via double pinning . . . . .	36

# Chapter 1

## Introduction to microresonator-based frequency combs

This chapter introduces the basic physics of optical frequency-comb generation in Kerr-nonlinear microring resonators, with a particular emphasis on providing context for the results described in the subsequent chapters. This field emerged in 2007 with the first report of comb generation in silica microtoroids [1], and has evolved rapidly. There are facets to the field that are not discussed here; we note that a number of papers that review this topic have been published, each of which provides a unique perspective [2–5]. The combs generated in Kerr-nonlinear ring resonators, excluding those generated in definitively ‘macro’ fiber loops, have generally been called microcombs, despite the fact that some of the resonators used to generate them have dimensions on the scale of several millimeters. Microcombs are an attractive technology because of their high repetition rates and small footprints, especially relative to modelocked-laser-based combs, which make them promising candidates for inclusion in integrated photonics systems. Microcomb generation has been reported in a variety of platforms, including the aforementioned silica microtoroids, silica wedge [6, 7] and rod [8] resonators, crystalline magnesium-fluoride [9] and calcium-fluoride [10] resonators, and silicon-nitride waveguide resonators [11, 12], which have the advantage of being immediately amenable to photonic integration.

For simplicity, and following the terminology of the field, we will refer to broadband optical spectra generated through frequency conversion in Kerr-nonlinear microring resonators as ‘Kerr combs,’ even when the output is not strictly a coherent frequency comb. Finally, we note that although researchers have so far focused on Kerr-comb generation with the ring geometry, it is also possible to generate Kerr combs in a Kerr-nonlinear Fabry-Perot (FP) cavity, as has been demonstrated in several experiments [13, 14]. Theoretical investigations of Kerr-comb generation with the FP geometry are presented in Chapter 2.

### 1.1 Optical microring resonators

An optical microring resonator guides light for many round trips around a closed path in a dielectric medium by total internal reflection. The principle is the same as the guiding of light in an optical fiber, and indeed a ‘macroring’ resonator can be constructed from a loop of fiber, using a fiber-optic coupler with a small coupling ratio as an input/output port. Microring resonators can be constructed by looping an optical waveguide back on itself, in which case the resonator provides index contrast and light confinement over a full 360° of the modal cross-section. Alternatively, resonators can be realized with geometries that lack an inner radius dimension and therefore provide less spatial confinement. In this case they can host ‘whispering-gallery modes,’<sup>1</sup> so-called due to their similarity with the acoustic ‘whispering-gallery’ waves that permit a listener on one side of St. Paul’s cathedral (for example) to hear whispers uttered by a speaker on the other side of the cathedral. A schematic

<sup>1</sup> In some sources the terminology ‘whispering-gallery mode resonator’ has been applied more generally, but the analogy to the acoustic case seems most appropriate for resonators in which index contrast is not provided over a full 360° of the modal cross-section. Otherwise it is unclear what makes a WGM resonator different from a fiber loop, which in the limit of large radius obviously does not host whispering-gallery modes. This issue of terminology is discussed in Ref. [15].

depiction of the basic components of a typical microring-resonator experiment is shown in Fig. 1.1. Optical microring resonators have a host of characteristics that make them useful for photonics applications in general and for nonlinear optics in particular; these include the ease with which they can be integrated and the ability to tailor the spectral distribution of guided modes through careful resonator design, as well as the ultra-high quality factors that have been demonstrated ( $\geq$  several hundred million). The resonator quality factor  $Q$  is defined as  $Q = \omega_0\tau_{ph} = \nu_0/\Delta\nu$ , where  $\omega_0 = 2\pi\nu_0$  is the optical angular frequency,  $\tau_{ph}$  is the photon lifetime, and  $\Delta\nu$  is the resonance linewidth. The  $Q$  can be interpreted literally as the optical phase that is traversed by the carrier wave during the photon lifetime and is a useful figure of merit for nonlinear optics.

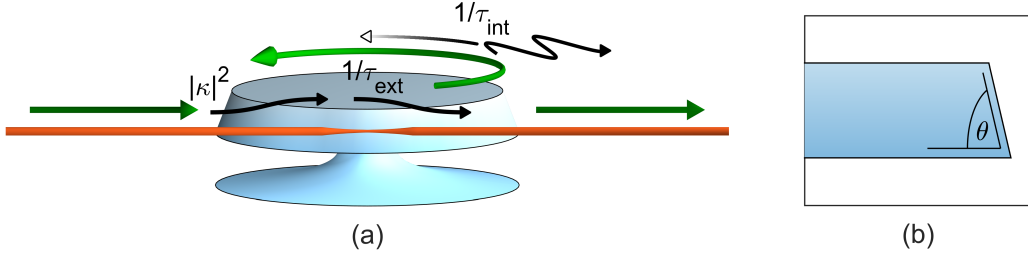


Figure 1.1: **Optical microdisk resonator.** (a) An optical microring resonator with the disk geometry as described in Ref. [6], operated in a through-coupled configuration. Light (green) is evanescently coupled into and out of the resonator through a tapered optical fiber, shown in orange, which contacts the resonator near the fiber’s point of smallest diameter. Light circulates in whispering-gallery modes concentric to the resonator’s circumference. The black labels indicate the coupling and loss rates discussed in Sec. 1.1.1:  $|\kappa|^2$  is the rate at which incoming photons are coupled into the resonator,  $1/\tau_{ext}$  is the rate at which circulating photons are coupling into the waveguide, and  $1/\tau_{int}$  is the intrinsic loss rate. Here contributions to  $1/\tau_{int}$  from absorption and radiative losses are depicted. (b) The wedge angle  $\theta$  can be adjusted to control the geometric dispersion of the propagating whispering-gallery modes as described in Ref. [16], as  $\theta$  dictates, for example, the extent to which larger (longer-wavelength) modes are confined further from the circumference of the wedge.

A microring resonator supports propagating guided modes of electromagnetic radiation with (vacuum) wavelengths that evenly divide the optical round-trip path length:  $\lambda_m = n_{eff}(\lambda_m)L/m$ , with associated resonance frequencies  $\nu_m = c/\lambda_m = mc/n_{eff}(\nu_m)L$ . This leads to constructive interference from round trip to round trip. Here  $m$  is the azimuthal mode number and the quantity  $Ln_{eff}(\lambda_m)$  is the optical round-trip path length of the mode, where  $n_{eff}(\lambda_m)$  defines an effective index of refraction related to the mode’s propagation constant  $k(\omega)$  via  $k(\omega) = n_{eff}(\omega)\omega/c$  (see e.g. Refs. [17, 18]; we use the symbol  $k$  here and reserve the standard symbol  $\beta$  for another quantity). The free-spectral range  $f_{FSR}$  of a resonator is the *local* frequency spacing between modes, calculated via:

$$f_{FSR} \approx \frac{\nu_{m+1} - \nu_{m-1}}{2} \quad (1.1)$$

$$= \frac{\partial \nu_m}{\partial m} \quad (1.2)$$

$$= \frac{c}{n_{eff}(\nu)L} - \frac{mc}{n_{eff}^2(\nu)L} \frac{\partial n_{eff}}{\partial \nu} \frac{\partial \nu}{\partial m}, \quad (1.3)$$

so that, rearranging, we obtain:

$$f_{FSR} = \frac{c/L}{\left(n_{eff} + \nu \frac{\partial n_{eff}}{\partial \nu}\right)} = \frac{c}{n_g L} = 1/T_{RT}, \quad (1.4)$$

where  $n_g = n_{eff} + \nu \frac{\partial n_{eff}}{\partial \nu}$  is the group velocity of the mode and  $T_{RT}$  is the mode's round-trip time. The effective index  $n_{eff}$  is frequency dependent due to both intrinsic material dispersion and geometric dispersion, where the latter results for example from different sampling of material properties for different wavelength-dependent mode areas. A frequency-dependent  $n_{eff}$  leads to a non-uniform spacing in the cavity modes in frequency despite the linearity of  $\nu_m$  in  $m$ ; equivalently this results in a frequency dependence of  $n_g$  and  $f_{FSR}$ .

Depending on the design, microring resonators can support many transverse mode profiles, or just one. The former is typical of whispering-gallery-mode resonators that lack an inner radius, such as the wedge resonator shown in Fig. 1.1 or free-standing silica microrod resonators [8]; the latter can be readily achieved using chip-integrated single-mode photonic waveguides. For a given resonator geometry, to calculate the frequency-dependent effective index  $n_{eff}(\nu)$ , thereby enabling calculation of the resonance frequencies and wavelengths, one must solve Maxwell's equations for the resonator geometry. Except in special cases of high symmetry (e.g. a dielectric sphere [19]), this is typically done numerically using finite-element modeling tools like COMSOL. The modes of an optical resonator, both within a mode family defined by a transverse mode profile (such that they differ only by azimuthal mode number  $m$ ) and between mode families, must be orthogonal [20], with no linear coupling between them.

### 1.1.1 Resonant enhancement in a microring resonator

The lifetime  $\tau_{ph}$  of circulating photons in a resonator is fundamental to its fitness for applications. Generally, two processes lead to the loss of circulating photons: intrinsic dissipation that occurs at a rate  $1/\tau_{int}$  and out-coupling to an external waveguide that occurs at a rate  $1/\tau_{ext}$ , leading to a total loss rate of  $\tau_{ph}^{-1} = \tau_{ext}^{-1} + \tau_{int}^{-1}$ . To understand the quantitative role of these parameters, we consider a cavity mode of frequency  $\omega_0$  and described by instantaneous amplitude  $a(t)$  (normalized such that  $|a|^2 = N$ , the number of circulating photons) driven by a pump field with frequency  $\omega_p$  and rotating amplitude  $s \propto \exp(i\omega_p t)$  (normalized such that  $|s|^2 = S$ , the rate at which photons in the coupling waveguide pass the coupling port) that is in-coupled with strength  $\kappa$ . The equation of motion for such a system is [20]:

$$\frac{da}{dt} = i\omega_0 a - \left( \frac{1}{2\tau_{int}} + \frac{1}{2\tau_{ext}} \right) a + \kappa s, \quad (1.5)$$

and the rates that determine the evolution of  $a$  are shown schematically in Fig. 1.1. We can immediately solve this equation by assuming that  $a \propto \exp(i\omega_p t)$ , and we obtain:

$$a = \frac{\kappa s}{\left( \frac{1}{2\tau_{int}} + \frac{1}{2\tau_{ext}} \right) + i(\omega_p - \omega_0)}. \quad (1.6)$$

The coupling strength  $\kappa$  into the waveguide and the out-coupling rate  $1/\tau_{ext}$  are related by  $|\kappa|^2 = 1/\tau_{ext}$ ; one can arrive at this conclusion by considering the special case  $1/\tau_{int} = 0$  and exploiting the time-reversal symmetry of the system under this condition [20]. By squaring Eq. 1.6 and inserting this relationship between  $\kappa$  and  $\tau_{ext}$ , we find:

$$N = \frac{\Delta\omega_{ext} S}{\Delta\omega^2/4 + (\omega_p - \omega_0)^2}, \quad (1.7)$$

where we have defined the rates  $\Delta\omega_{ext} = 1/\tau_{ext}$ ,  $\Delta\omega_{int} = 1/\tau_{int}$ , and  $\Delta\omega = \Delta\omega_{ext} + \Delta\omega_{int}$ . Two important observations can be drawn from Eq. 1.7: First, the cavity response is Lorentzian with a full-width at half-maximum (FWHM) linewidth that is related to the photon lifetime via  $\tau_{ph} = 1/\Delta\omega$ , and second, on resonance the number of circulating photons is related to the input rate by the factor  $\Delta\omega_{ext}/\Delta\omega^2 \ll 1$ . This factor is not yet the resonant enhancement, which we now

calculate by considering the circulating power  $P = N\hbar\omega_p/T_{RT}$  on resonance (when  $\omega_p = \omega_0$ ):

$$P = \frac{4\Delta\omega_{ext}P_{in}/T_{RT}}{\Delta\omega^2} \quad (1.8)$$

$$= \frac{2}{\pi} P_{in}\eta\mathcal{F}, \quad (1.9)$$

where  $\mathcal{F} = 2\pi\tau_{ph}/T_{RT} = f_{FSR}/\Delta\nu$  is the resonator finesse,  $\eta = \Delta\omega_{ext}/\Delta\omega$  is the coupling ratio, typically of order  $\sim \frac{1}{2}$ , and  $P_{in} = \hbar\omega_p S$  is the power in the waveguide. Thus, the circulating power is approximately a factor  $\mathcal{F}$  greater than the input power. The combination of this resonant enhancement and a small cavity mode volume enables very large circulating optical intensities in high finesse resonators, which is important for the application of microresonators in nonlinear optics.

### 1.1.2 Thermal effects in microresonators

In a typical microresonator frequency-comb experiment, a frequency-tunable pump laser is coupled evanescently into and out of the resonator using a tapered optical fiber [21, 22] (for e.g. free-standing silica disc resonators) or a bus waveguide (for chip-integrated resonators, e.g. in silicon nitride rings). When spatial overlap and phase-matching ( $n_{eff,res} \sim n_{eff,coupler}$  [23]) between the evanescent mode of the coupler and a whispering-gallery mode of the resonator is achieved, with the frequency of the pump laser close to the resonant frequency of that mode, light will build up in the resonator and the transmission of the pump laser past the resonator will decrease.

In any experiment in which a significant amount of pump light is coupled into a resonator, one immediately observes that the cavity resonance lineshape in a scan of the pump-laser frequency is not Lorentzian as expected from Eq. 1.7; plots of measured resonance lineshapes are shown in Fig. 1.2a. This is because the resonator heats as it absorbs circulating optical power. Associated with this change in temperature are changes in the mode volume and the refractive index, described respectively by the coefficient of thermal expansion  $\partial V/\partial T$  and the thermo-optic coefficient  $\partial n/\partial T$ . For typical microresonator materials the thermo-optic effect dominates, and  $\partial n/\partial T > 0$  leads to a decrease in the resonance frequency with increased circulating power in thermal steady state. Thus, for an adiabatic scan across the cavity resonance with decreasing laser frequency, as the laser approaches the resonance in frequency space and power is coupled into the resonator, the resonance frequency will begin to shift with the laser frequency, and a sawtooth-shaped resonance emerges.

The thermal dynamics related to  $\partial n/\partial T$  and  $\partial V/\partial T$  dictate the signs and values of detuning  $\omega_0 - \omega_p$  that are readily accessible in experiment. Specifically, a calculation of the thermal dynamics of the system composed of the pump laser and the resonator reveals that when the pump laser with frequency  $\omega_p$  is near the ‘cold-cavity’ resonance frequency of a given cavity mode  $\omega_{0,cold}$  the resonance has three possible thermally-shifted resonance frequencies  $\omega_{0,shifted}$  at which thermal steady state is achieved [24]. Generally, these points are:

- (1)  $\omega_p > \omega_{0,shifted}$ , blue detuning<sup>2</sup> with significant coupled power and thermal shift
- (2)  $\omega_p < \omega_{0,shifted}$ , red detuning with significant coupled power and thermal shift
- (3)  $\omega_p \ll \omega_0$ , red detuning with insignificant coupled power and insignificant thermal shift

These points are depicted schematically in Fig. 1.2b. Steady-state point (1) is experimentally important, because in the presence of pump-laser frequency and power fluctuations it leads to so-called thermal ‘self-locking.’ Specifically for steady-state point (1), this can be seen as follows:

- If the pump-laser power increases, the cavity heats, the resonance frequency decreases, the detuning increases, and the change in coupled power is minimized.
- If the pump-laser power decreases, the cavity cools, the resonance frequency increases, the detuning decreases, and the change in coupled power is minimized.

---

<sup>2</sup> Here we use the convention that the ‘color’ of the detuning specifies the position of the laser with respect to the resonance—‘blue’ detuning means that the laser is more blue, or higher in frequency.

- If the pump-laser frequency increases, the cavity cools, the resonance frequency increases, and the change in coupled power is minimized.
- If the pump-laser frequency decreases, the cavity heats, the resonance frequency decreases, and the change in coupled power is minimized.

This is in contrast with steady-state point (2), where each of the four pump-laser fluctuations considered above generates a positive feedback loop, with the result that any fluctuation will push the system towards point (1) or point (3) and so point (2) is unstable. This preference of the system to occupy point (1) or point (3) over a range of pump-laser detuning is referred to as thermal bistability. As a result of this bistability, point (2) (i.e. red detuning with significant coupled power) cannot be observed in an experimental scan of the pump laser across the resonance in either direction. As explained above, when the pump-laser frequency is decreased the resonance takes on a broad sawtooth shape, while in an increasing-frequency scan the resonance takes on a narrow pseudo-Lorentzian profile whose exact shape depends on the scan parameters relative to the thermal timescale. A second consequence is that, in the absence of other stabilizing effects, operation at red detuning with significant coupled power in a microresonator experiment requires special efforts to mitigate the effects of thermal instability.

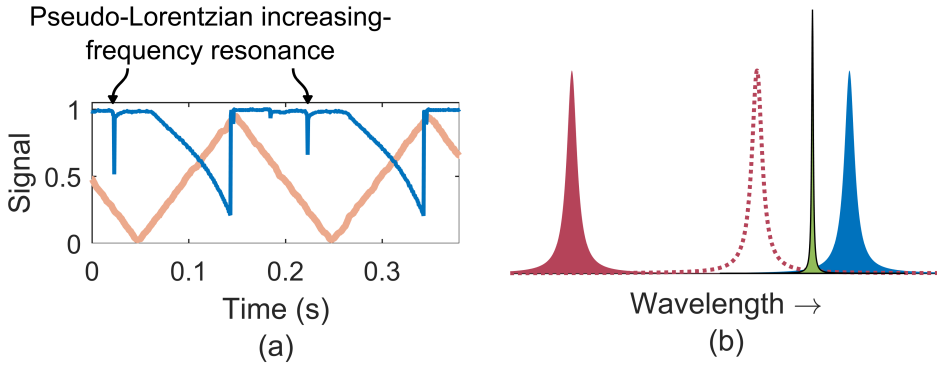


**Figure 1.2: Thermal bistability in microresonators.** (a) Measurement of power transmitted past the microresonator (blue) in an experiment using a  $\sim 16.5$  GHz-FSR microdisk resonator and a tapered fiber. The wavelength of the pump laser is controlled by a piezo-electric crystal that adjusts the length of the laser cavity. Here, larger control signal (orange) corresponds to longer laser wavelength. As the laser wavelength is increased, the resonator heats and a sawtooth-shaped resonance is observed. Ultimately the resonator reaches a maximum temperature that depends on the pump power, and the laser then becomes red-detuned as the wavelength continues to increase; then the resonator rapidly cools and the resonance is lost. Shortly thereafter, the direction of the scan is reversed. As the resonator wavelength is decreased, the system will ‘flip’ from steady-state point (3) to steady-state point (1), leading to observation of a narrow pseudo-Lorentzian resonance, with the exact shape depending on the thermal and scanning timescales. (b) Depiction of the three steady-state points for the laser detuning. For fixed laser wavelength (green), stable steady-state points exist with relatively small blue detuning and significant coupled power (solid blue), and relatively large red detuning and little coupled power (solid red). An unstable steady-state point also exists with red detuning and significant coupled power (dashed red). Note in this terminology that the color of the detuning (red or blue) refers to the position of the laser relative to the position of the resonance in wavelength space.

## 1.2 Microring resonator Kerr frequency combs

The high circulating optical intensities accessible in resonators with long photon lifetimes find immediate application in the use of microresonators for nonlinear optics. The experiments described in this thesis are conducted in silica microresonators. Silica falls into a broader class of materials that exhibit both centro-symmetry, which dictates that the second-order nonlinear susceptibility  $\chi^{(2)}$  must vanish, and a significant third-order susceptibility  $\chi^{(3)}$ . The  $n^{\text{th}}$ -order susceptibility is a term in the Taylor expansion describing the response of the medium's polarization to an external electric field [25]:  $P = P_0 + \epsilon_0 \chi^{(1)} E + \epsilon_0 \chi^{(2)} E^2 + \epsilon_0 \chi^{(3)} E^3 + \dots$ . The effect of  $\chi^{(3)}$  can be described in a straightforward way as a dependence of the refractive index on the local intensity [17],

$$n = n_0 + n_2 I \quad (1.10)$$

where  $n_2 = \frac{3\chi^{(3)}}{4n_0^2 \epsilon_0 c}$  is called the Kerr index [17, 26]. The intensity-dependence of the refractive index resulting from the third-order susceptibility  $\chi^{(3)}$  is referred to as the optical Kerr effect and enables the self-phase modulation (SPM), cross-phase modulation (XPM), and four-wave mixing (FWM) nonlinear processes [25]. Four-wave mixing is a general frequency-domain description of an energy-conserving interaction between fields of up to four different frequencies, as depicted in Figs. 1.3a and b; self-phase modulation and cross-phase modulation can be thought of as time-domain descriptions of particular cases of FWM. In SPM and XPM the nonlinear interaction leads to intensity-dependent phase shifts of the field. If the intensity varies in time, for example in the case of an optical pulse, then the resulting time-varying nonlinear phase shift corresponds to the application of a chirp to the pulse. This can lead to modification of the pulse's spectrum, including the generation of new frequency components.<sup>3</sup>

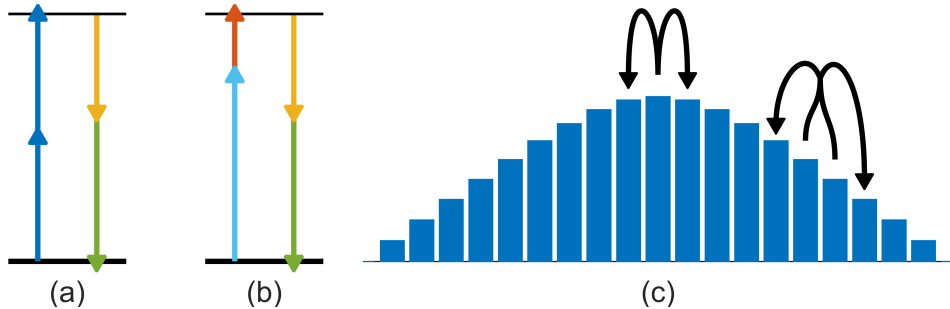


**Figure 1.3: An illustration of four-wave mixing and frequency-comb generation.** (a) Degenerate four-wave mixing, in which two fields of the same frequency  $\omega_1$  (blue) mix and generate fields at two new frequencies  $\omega'$  and  $\omega''$  (yellow and green). The schematic indicates the energy-conservation requirements of the process, which can be written as  $2\omega_1 = \omega' + \omega''$ . (b) Non-degenerate four-wave mixing, in which two fields of different frequencies  $\omega_2$  and  $\omega_3$  (light blue and orange) mix to generate fields at frequencies  $\omega'$  and  $\omega''$  (yellow and green). Energy conservation is now expressed as  $\omega_2 + \omega_3 = \omega' + \omega''$ . (c) Schematic depiction of one degenerate FWM step and one non-degenerate FWM step in a cascaded four-wave mixing process that generates a frequency comb. Figure after Ref. [2].

For FWM to efficiently lead to the generation of new frequencies in some medium or waveguide it must be effectively phasematched, meaning that the quantity

$$\Delta k = k(\omega_1) + k(\omega_2) - k(\omega') - k(\omega''), \quad (1.11)$$

---

<sup>3</sup> SPM doesn't always lead to the generation of new frequency components. For example, solitons can propagate without becoming chirped through a balance between SPM and dispersion, and SPM can even lead to narrowing of the bandwidth of a pulse when e.g. the chirp generated by SPM has sign opposite to an existing chirp on the pulse.

where  $k(\omega) = n_{eff}(\omega)\omega/c$  is the propagation constant, should be made as small as possible; in the above the four frequencies correspond to those depicted in Figs. 1.3a and b. In a ring resonator, FWM is intrinsically phasematched in interactions between fields propagating in modes with azimuthal mode numbers  $m_1$ ,  $m_2$ ,  $m'$ , and  $m''$  such that  $m_1 + m_2 = m' + m''$ . Reports of few-mode parametric oscillation in microresonators based on FWM preceded the first observations of Kerr-comb generation [27–29].

In 2007, the remarkable observation by Del’Haye et al. of *cascaded four-wave mixing* (CFWM, shown in Fig. 1.3c) in anomalously-dispersive ( $k'' = \frac{\partial^2}{\partial\omega^2}\frac{n_{eff}(\omega)\omega}{c} < 0$ ) toroidal silica microcavities on silicon chips brought about a new era for frequency comb research. They observed the generation many co-circulating optical fields that were uniformly spaced by  $f_{rep}$  ranging from 375 GHz to  $\sim 750$  GHz (depending on the platform) [1]. This result showed that the non-uniform distribution of cavity resonance frequencies due to dispersion could be overcome to generate an output with many equidistant frequency modes. A second important development occurred in 2012, when Herr et al. reported the generation of frequency combs corresponding in the time domain to single circulating optical ‘soliton’ pulses [30, 31]. This observation followed the observation of solitons in formally-equivalent passive fiber-ring resonators in 2010 [32]. Due to unique properties that make them particularly well-suited for applications, as discussed in Sec. 1.3.3, the generation and manipulation of soliton combs has become a significant priority in microcomb research.

### 1.2.1 A model for Kerr-comb nonlinear optics: The Lugiato-Lefever equation

Kerr-comb generation can be motivated and partially understood through the CFWM picture [33], but the phase and amplitude degrees of freedom for each comb line mean that CFWM gives rise to a rich space of comb phenomena—it is now known that Kerr combs can exhibit several fundamentally distinct outputs. A useful model for understanding this rich space is the Lugiato-Lefever equation (LLE), which was shown to describe microcomb dynamics by Chembo and Menyuk [34] through Fourier-transformation of a set of coupled-mode equations describing CFWM and by Coen, Randle, Sylvestre, and Erkintalo [35] through time-averaging of a more formally-accurate model for a low-loss resonator (as first performed by Haelterman, Trillo, and Wabnitz [36]). The LLE is a nonlinear partial-differential equation that describes evolution of the normalized cavity field envelope  $\psi$  over a slow time  $\tau = t/2\tau_{ph}$  in a frame parametrized by the ring’s azimuthal angle  $\theta$  (running from  $-\pi$  to  $\pi$ ) co-moving at the group velocity.<sup>4</sup> A derivation of the LLE is provided in Appendix ???. The equation in the notation of Chembo and Menyuk, as it will be used throughout this thesis, reads:

$$\frac{\partial\psi}{\partial\tau} = -(1 + i\alpha)\psi + i|\psi|^2\psi - i\frac{\beta_2}{2}\frac{\partial^2\psi}{\partial\theta^2} + F. \quad (1.12)$$

This equation describes  $\psi$  over the domain  $-\pi \leq \theta \leq +\pi$  with periodic boundary conditions  $\psi(-\pi, \tau) = \psi(\pi, \tau)$ . Here  $F$  is the field strength of the pump laser, with  $F$  and  $\psi$  both normalized so that they take the value 1 at the absolute threshold for parametric oscillation:  $F = \sqrt{\frac{8g_0\Delta\omega_{ext}}{\Delta\omega^3}\frac{P_{in}}{\hbar\omega_p}}$ ,  $|\psi|^2 = \frac{2g_0T_{RT}}{\hbar\omega_p\Delta\omega}P_{circ}(\theta, \tau)$ , so that  $|\psi(\theta, \tau)|^2$  is the instantaneous normalized power at the co-moving azimuthal angle  $\theta$ . Here  $g_0 = n_2c\hbar\omega_p^2/n_g^2V_0$  is a parameter describing the four-wave mixing gain,  $\Delta\omega_{ext}$  is the rate of coupling at the input/output port,  $\Delta\omega = 1/\tau_{ph}$  is the FWHM resonance linewidth,  $P_{in}$  is the pump-laser power,  $P_{circ}(\theta, \tau)$  is the local circulating power in the cavity,  $\hbar$  is Planck’s constant, and  $\omega_p$  is the pump-laser frequency. The parameters  $n_2$ ,  $n_g$ , and  $V_0$  describe the nonlinear (Kerr) index (see Eqn. 1.10), the group index of the mode, and the effective nonlinear mode volume at the pump frequency;  $L$  is the physical round-trip length of the ring cavity.

The parameters  $\alpha$  and  $\beta_2$  describe the frequency detuning of the pump laser and second-order dispersion of the resonator mode family into which the pump laser is coupled, both normalized to

<sup>4</sup> The co-moving azimuthal angle  $\theta$  is analogous to the ‘fast time’ variable that appears in, for example, the nonlinear Schrodinger equation for fiber-optic pulse propagation [17], and it can be transformed explicitly to a fast time  $t$  via  $t = T_{RT} \times \frac{\theta}{2\pi}$ .

half the cavity linewidth:

$$\alpha = -\frac{2(\omega_p - \omega_0)}{\Delta\omega}, \quad (1.13)$$

$$\beta_2 = -\frac{2D_2}{\Delta\omega}; \quad (1.14)$$

here  $D_2 = \left. \frac{\partial^2 \omega_\mu}{\partial \mu^2} \right|_{\mu=0}$  is the second-order modal dispersion parameter, where  $\mu$  is the pump-referenced mode number of Eq. ???. The parameters  $D_1 = \left. \frac{\partial \omega_\mu}{\partial \mu} \right|_{\mu=0} = 2\pi f_{FSR}$  and  $D_2$  are related to the derivatives of the propagation constant  $k(\omega) = \frac{n_{eff}(\omega)\omega}{c}$  via  $D_1 = 2\pi/Lk'$  and  $D_2 = -D_1^2 \frac{k''}{k'}$ . It is useful to note that  $k' = 1/v_g$ , where  $v_g$  is the group velocity in the medium, and  $k''$  is often referred to as the GVD parameter and denoted by  $\beta_2$ , which here is reserved for the dispersion parameter in the LLE. Expressions for higher-order modal dispersion parameters  $D_n$  in terms of the expansion of the propagation constant can be obtained by evaluating the equation  $D_{n>1} = (D_1 \frac{\partial}{\partial \omega})^{n-1} D_1$ , and may be incorporated into the LLE up to desired order  $N$  through the replacement:

$$-i \frac{\beta_2}{2} \frac{\partial^2 \psi}{\partial \theta^2} \rightarrow + \sum_{n=1}^N i^{n+1} \frac{\beta_n}{n!} \frac{\partial^n \psi}{\partial \theta^n}, \quad (1.15)$$

where  $\beta_n = -2D_n/\Delta\omega$ . This thesis describes frequency-comb generation in anomalously-dispersive resonators, and so  $\beta_2 < 0$  throughout.

The formulation of the LLE in terms of dimensionless normalized parameters helps to elucidate the fundamental properties of the system and facilitates comparison of results obtained in platforms with widely different experimental conditions. The LLE relates the time-evolution of the intracavity field (normalized to its threshold value for cascaded four-wave mixing) to the power of the pump laser (normalized to its value at the threshold for cascaded four-wave mixing), the pump-laser detuning (normalized to half the cavity linewidth), and the cavity second-order dispersion quantified by the change in the FSR per mode (normalized to half the cavity linewidth). One example of the utility of this formulation is that it makes apparent the significance of the cavity linewidth in determining the output comb, and underscores the fact that optimization of the dispersion, for example, without paying heed to the effect of this optimization on the cavity linewidth, may not yield the desired results. This adds an additional layer of complexity to dispersion engineering relative to straight waveguides.

The LLE is, of course, a simplified description of the dynamics occurring in the microresonator. It abstracts the nonlinear dynamics and generally successfully describes the various outputs that can be generated in a microresonator frequency comb experiment. The LLE is a good description of these nonlinear dynamics when the resonator photon lifetime, mode overlap, and nonlinear index  $n_2$  are roughly constant over the bandwidth of the generated comb, and when the dominant contribution to nonlinear dynamics is simply the self-phase modulation term  $i|\psi|^2\psi$  arising from the Kerr nonlinearity. The LLE neglects the polarization of the electric field ( $\psi$  is a scalar), as well as thermal effects and the Raman scattering and self-steepening nonlinearities, although in principle each of these can be included [17, 31, 37, 38]. It is also worth emphasizing that the LLE can be derived from a more formally-accurate Ikeda map (as explained by Coen et al. [35]), in which the effect of localized input- and output-coupling is included in the model. This derivation is accomplished by ‘delocalizing’ the pump field and the output-coupling over the round trip, including only their averaged effects. This is an approximation that is valid in the limit of high finesse due to the fact that the cavity field cannot change on the timescale of a single round trip, but as a result the LLE necessarily neglects all dynamics that might have some periodicity at the round-trip time; the fundamental timescale of LLE dynamics is the photon lifetime.

### 1.3 Description of Kerr-comb outputs using the Lugiato-Lefever equation

The LLE provides a useful framework for the prediction and interpretation of experimental results. Basically, it predicts the existence of two fundamentally distinct types of Kerr-combs: extended temporal patterns and localized soliton pulses. These predictions are born out by experiments, the interpretation of which is facilitated by insight gained from the LLE. In the remainder of this chapter I briefly present some analytical results that can be obtained from the LLE about the behavior of the continuous-wave (CW) field that exists in the resonator in the absence of Kerr-comb formation, and then discuss these two types of comb outputs. This discussion provides context for the results presented in the next two chapters. Fig. 1.4 summarizes the results that will be presented in the remainder of this chapter, and in particular shows the values of the parameters  $\alpha$  and  $F^2$  at which solitons and extended patterns can be obtained.

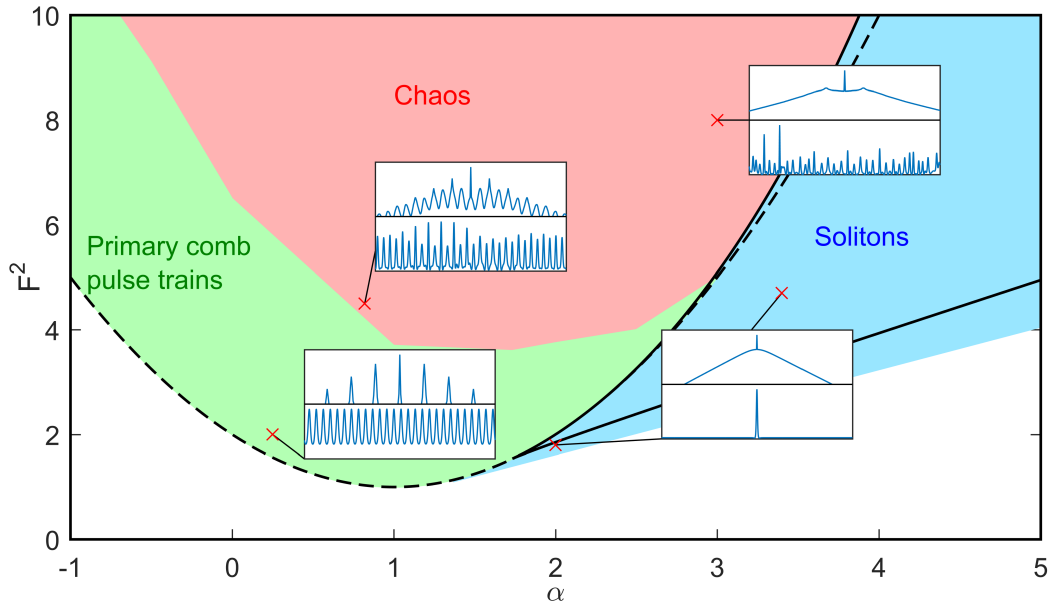


**Figure 1.4: Solution space for the Lugiato-Lefever equation.** Depiction of the various behaviors exhibited by  $\psi$  as a function of its position in the  $\alpha - F^2$  plane; this predicts the type of Kerr-comb output as a function of the pump-laser detuning and power, the parameters that are most readily adjusted in experiment. Curves plotted in black are obtained through analytical investigation of the LLE; these include the threshold curve for parametric oscillation (dashed black, Eq. 1.22) and the lines obtained via  $\rho(\alpha, F^2) = \rho_{\pm}(\alpha)$  (solid black, Eq. 1.19), which define the region where the LLE exhibits multiple flat solutions (i.e. solutions such that  $\partial\psi/\partial\theta = 0$ , Eq. 1.16). Extended patterns arise above the threshold curve through modulation instability. Solitons exist outside of the threshold curve at higher red detuning, up to an approximate maximum  $\alpha_{max} = \pi^2 F^2/8$ . The lines bounding the existence of chaos are not known precisely, and in fact chaos can be observed in simulation outside of the threshold curve at values  $\alpha > \alpha_{thresh,+}$  (Eq. 1.23). Insets show representative simulation results for the various types of comb outputs in the frequency (top) and time (bottom) domains. Fig. after Ref. [39].

#### 1.3.1 Analytical investigation of the resonator's CW response

Some insight into comb dynamics can be obtained via analytical investigations of the LLE, Eq. 1.12. This section largely follows the analysis of Ref. [39], with similar analysis having been performed elsewhere, for example in Refs. [35] and [40]. When the derivative term  $\partial^2\psi/\partial\theta^2$  in

the LLE is non-zero,  $\psi$  is necessarily broadband, and a Kerr comb has been formed. There are no known exact analytical solutions to the LLE to describe Kerr-comb outputs, which must instead be numerically simulated (see Appendix ??). However, flat solutions  $\psi_{CW}$  to the LLE may be calculated by setting all derivatives to zero—when these solutions can be realized physically (discussed below), they describe a CW field in the resonator. Upon setting the derivatives in the LLE to zero, one finds:

$$F = (1 + i\alpha)\psi_{CW} - i|\psi_{CW}|^2\psi_{CW}. \quad (1.16)$$

The circulating intensity  $\rho = |\psi_{CW}|^2$  is obtained by taking the modulus-square of Eq. 1.16 to obtain:

$$F^2 = (1 + (\alpha - \rho)^2) \rho, \quad (1.17)$$

$$= \rho^3 - 2\alpha\rho^2 + (\alpha^2 + 1)\rho, \quad (1.18)$$

whereupon this equation can be numerically solved for  $\rho$ . As a third-order polynomial in  $\rho$  this equation has three solutions, one or three of which may be real; the complex solutions are unphysical. The function  $F^2(\alpha, \rho)$  defined by this equation uniquely determines  $F^2$  given  $\alpha$  and  $\rho$ . We now consider plotting a graph of  $F^2(\alpha, \rho)$  with  $\alpha$  held constant; examples are given in Fig. 1.5. By noting that  $F^2(\alpha, \rho = 0) = 0$  and  $\partial F^2/\partial\rho|_{\rho=0} > 0$ , we can conclude that a graph of  $F^2(\alpha, \rho)$  will cross the same value  $F^2$  three times if  $F^2$  is between the extremal values  $F_{\pm}^2(\alpha)$  at which  $\partial F^2/\partial\rho = 0$ . This means that three real solutions  $\rho_1$ ,  $\rho_2$ , and  $\rho_3$  for the inverted function  $\rho(\alpha, F^2)$  exist for each value of  $F^2$  between  $F_-^2(\alpha)$  and  $F_+^2(\alpha)$ . The values  $F_{\pm}^2(\alpha)$  bounding this region of degeneracy in  $\rho$  are found by inserting the values  $\rho_{\pm}$  at which  $\partial F^2/\partial\rho = 0$  into Eq. 1.17. That is,  $F_{\pm}^2(\alpha) = F^2(\alpha, \rho_{\mp})$ , where:

$$\rho_{\pm} = \frac{2\alpha \pm \sqrt{\alpha^2 - 3}}{3}. \quad (1.19)$$

For pump powers outside of the interval  $[F_-^2(\alpha), F_+^2(\alpha)]$ , which varies with  $\alpha$ , there is only one real solution  $\rho$ ; within this interval there are three. This is illustrated in Fig. 1.5. The smallest value of  $F^2$  at which the stationary curve  $\rho$  becomes multivalued is found to be  $F^2 = 8\sqrt{3}/9$  by solving for  $\rho_- = \rho_+$  and inserting the corresponding values into Eq. 1.17.

Physically, the coexistence of multiple flat solutions  $\rho$  at a given point  $(\alpha, F^2)$  corresponds to a ‘tilting’ of the Lorentzian transmission profile of the cavity and leads to bistability, even before taking into account thermal effects. This is illustrated in Fig. 1.5. For flat solutions  $\rho$ , an effective Kerr-shifted detuning can be defined as  $\alpha_{eff} = \alpha - \rho$ . The effective detuning simply incorporates the Kerr nonlinearity into the round-trip phase shift that describes the constructive or destructive interference of the circulating field with the pump at the coupling port. By noting that  $\alpha = F^2 = \rho$  solves Eq. 1.17, we can conclude that the position of the effective Kerr-shifted resonance is on the line  $\alpha = F^2$ , where  $\alpha_{eff} = 0$ .

Once the circulating intensity  $\rho$  is known, the corresponding flat solution  $\psi_{CW}$  can be determined from Eq. 1.16 by inserting the known value of  $\rho$  and solving for  $\psi_{CW}$ , with the result:

$$\psi_{CW} = \frac{F}{1 + i(\alpha - \rho)}. \quad (1.20)$$

This expression reveals that the flat solution acquires a phase  $\phi_s = \tan^{-1}(\rho - \alpha)$  relative to the pump.

If the flat solution(s) at a point  $(\alpha, F^2)$  is (are) unstable, a Kerr comb will form spontaneously. Stability analysis of the flat solutions can be performed, and for the case of second-order dispersion alone the results are [39]:

- In the region of multi-stability, if the flat solutions are ordered with increasing magnitude as  $\rho_1$ ,  $\rho_2$ , and  $\rho_3$ , the middle solution  $\rho_2$  is always unstable.
- When  $\alpha < 2$ , a flat solution  $\rho$  that is not the middle solution is stable if  $\rho < 1$ ; otherwise it is unstable. When the flat solution is unstable, the mode that experiences the greatest

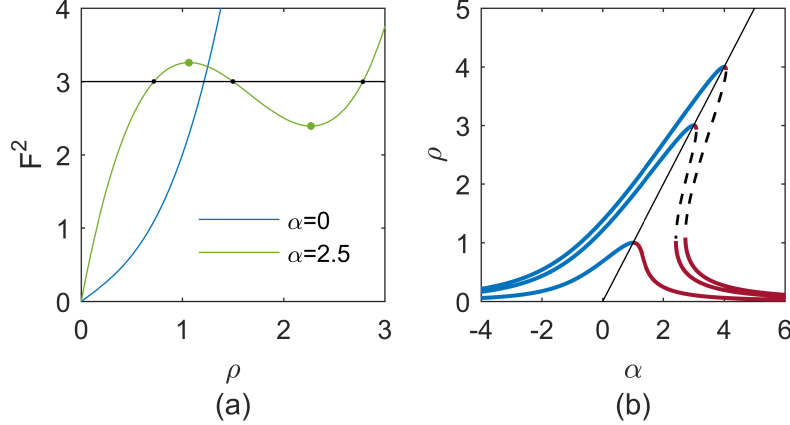


**Figure 1.5: Investigation of the circulating CW power in a Kerr resonator.** (a) Plots of  $F^2$  as a function of  $\rho$  for  $\alpha = 0$  (blue) and  $\alpha = 2.5$  (green), according to Eq. 1.17. When real values of  $\rho$  exist that extremize  $F^2$  according to this equation, multiple real solutions for the circulating power  $\rho$  exist between these extremal values of  $F^2$ . For  $\alpha = 2.5$  we indicate the extremal values of  $F^2$  as green dots. For an example value  $F^2 = 3$ , the corresponding allowed values  $\rho_1$ ,  $\rho_2$ , and  $\rho_3$  are the intersections of the green curve and the black line (black dots); such a line would have three intersections with the green curve for any value of  $F^2$  between  $F_\alpha^2(\rho_-)$  and  $F_\alpha^2(\rho_+)$ . (b) Kerr-tilted resonances curves  $\rho(\alpha)$  for  $F^2 = 1$  (smallest),  $F^2 = 3$ , and  $F^2 = 4$  (largest). The line  $\rho = \alpha = F^2$  (solid black) marks the highest circulating power for a given input power  $F^2$  and separates the effectively blue-detuned and effectively red-detuned branches. When  $F^2 > 8\sqrt{3}/9$  (obtained by solving for  $\rho_+ = \rho_-$ , Eq. 1.19), the resonance becomes tilted steeply enough that an unstable middle branch (dashed black) exists.

instability has mode number given by:

$$\mu_{max} = \sqrt{\frac{2}{\beta_2}(\alpha - 2\rho)} \quad (1.21)$$

Therefore, the pump-laser threshold curve for Kerr-comb generation can be determined in the region  $\alpha < 2$  of the  $\alpha - F^2$  plane by setting  $\rho = 1$  in Eq. 1.16:

$$F_{thresh}^2 = 1 + (\alpha - 1)^2, \quad (1.22)$$

$$\alpha_{thresh,\pm} = 1 \pm \sqrt{F^2 - 1}. \quad (1.23)$$

These equations explicitly describe the point at which comb is generated in an experiment in which the pump power or detuning is varied while the other is held fixed.

### 1.3.2 Kerr comb outputs: extended modulation-instability patterns

Extended temporal patterns arise spontaneously as a result of the instability of the flat solution to the LLE when the pump laser is tuned above the threshold curve. Two types of extended patterns are shown in Fig. 1.6. These patterns can be stationary, in which case they are typically referred to as ‘Turing patterns’ or ‘primary comb,’ or can evolve in time, in which case they are typically referred to as ‘noisy comb’ or ‘spatiotemporal chaos.’ In general, the former occurs for lower values of the detuning  $\alpha$  and smaller pump strengths  $F^2$ ; although some studies of the transition from Turing patterns to chaos have been conducted (e.g. Ref. [41]), a well-defined boundary between the two has not been established, and may not exist.

In the spatial domain parametrized by  $\theta$ , a Turing pattern consists of a pulse train with (typically)  $n \gg 1$  pulses in the domain  $-\pi \leq \theta \leq \pi$ —the pulse train’s repetition rate is a multiple of the cavity FSR:  $f_{rep} = n \times f_{FSR}$ . Corresponding to the  $n$ -fold decreased period (relative to the round-trip time) of an  $n$ -pulse Turing pattern’s modulated waveform in the time domain, the optical spectrum of a Turing pattern consists of modes spaced by  $n$  resonator FSR—it is this widely-spaced spectrum that is referred to as ‘primary comb.’ Analytical approximations for Turing patterns are possible near threshold [42, 43] and in the small damping limit [44]. The stability analysis results from the last section can be used to predict the spacing  $n$  of a primary comb (equivalently the number of Turing-pattern pulses) generated in a decreasing-frequency scan across the resonance with fixed normalized pump power  $F^2$ :

$$n = \mu_{max,thresh} = \sqrt{\Delta\omega_0(1 + \sqrt{F^2 - 1})/D_2}, \quad (1.24)$$

which is obtained by inserting  $\alpha_{thresh,-}$  from Eq. 1.23 and  $\rho = 1$  into the expression for  $\mu_{max}$  in Eq. 1.21 above and moving to the dimensionful dispersion parameter  $D_2$ . Fig. 1.6a shows measured and simulated primary comb spectra and Fig. 1.6b shows the corresponding simulated time-domain waveform.

Spatiotemporal chaos can be understood as a Turing pattern whose pulses oscillate in height, with adjacent pulses oscillating out of phase. From such an oscillating Turing pattern, if  $\alpha$  and/or  $F^2$  is increased, one moves deeper into the chaotic regime and pulses begin to exhibit lateral motion and collisions; the number of pulses present in the cavity is no longer constant in time. Depending on the severity of the chaos (greater for larger  $\alpha$  and  $F^2$ ), a chaotic comb may correspond to a primary-comb-type spectrum with each primary-comb mode exhibiting sidebands at the resonator FSR, so-called ‘subcombs,’ or it may correspond to a spectrum with light in each cavity mode. Fig. 1.6c shows measured and simulated time-averaged spectra of chaotic combs and Fig. 1.6d shows a corresponding simulated time-domain waveform.

Relative to generation of solitons, discussed below, experimental generation of an extended pattern is straightforward. These patterns are generated with blue effective pump-laser detuning  $\alpha_{eff} < 0$ , where thermal locking can occur. Because they arise spontaneously from noise, their generation is (comparatively) straightforward: simply decrease the pump-laser frequency until a pattern is generated. Unfortunately, operation of a Kerr-comb in the extended pattern regime is disadvantageous for applications: the  $n$ -FSR spacing of primary comb presents a challenge for measurement of the repetition rate of the frequency comb due to the bandwidth of measurement electronics and is also an inefficient use of physical space (i.e. for an  $n$ -pulse primary comb pulse train, an equivalent pulse train can always be obtained using the single-soliton output of a resonator with area that is smaller by a factor of  $1/n^2$ ), and the aperiodic time-evolution of chaotic comb corresponds to modulation sidebands on the comb modes within the linewidth of the cavity that preclude the use of the comb as a set of stable optical reference frequencies.

An important property of these extended patterns is that they fill the resonator—the characteristic size of temporal features scales roughly as  $1/\sqrt{-\beta_2}$ , but these features are distributed densely and uniformly throughout the resonator. This means that the total circulating power of an extended pattern  $\int d\theta |\psi|^2$  is large relative to the localized pulses discussed in the next section, and therefore that extended patterns come with a comparatively large thermal shift of the resonance. As explained below, this contributes to the experimental challenges in soliton generation.

### 1.3.3 Kerr comb outputs: solitons

The term ‘soliton’ generally refers to a localized excitation that can propagate without changing its shape due to a delicate balance between dispersion (or diffraction) and nonlinearity; sometimes known as ‘solitary waves,’ solitons entered the scientific consciousness in the nineteenth century with their observation by John Scott Russell [45]. They are fundamental solutions to nonlinear partial-differential equations that describe a host of physical phenomena, and are found in several contexts within the field of nonlinear optics: spatial[42, 46] and spatiotemporal solitons (light bullets) [47] have been studied, and soliton modelocking [48, 49] is an important method of femtosecond

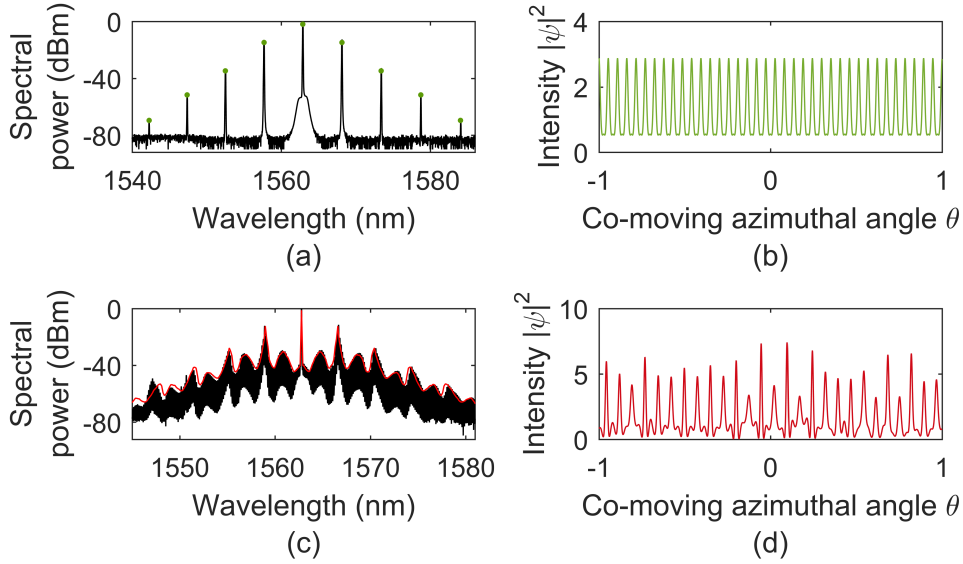


Figure 1.6: **Extended-pattern solutions to the LLE.** (a,b) Primary-comb pulse train in the frequency (a) and time (b) domains. The primary-comb spectrum corresponds to 39 time-domain pulses. The experimental optical spectrum (black) was obtained in a microdisk resonator with 17.32 GHz free-spectral range, and the simulation (green) is conducted with parameters near typical experimental values:  $F^2=6$ ,  $\alpha = -0.6$ , and  $\beta_2 = -0.0044$ . (c,d) Spatiotemporal chaos obtained in the same resonator. The experimental measurement (black) yields a time-averaged optical spectrum, with a simulation of qualitatively similar dynamics shown in red. Simulation parameters are  $F^2 = 4.2$ ,  $\alpha = 1.2$ , and  $\beta_2 = -0.0054$ . A snapshot of the evolving time-domain waveform is shown in (d).

pulse generation. Temporal Kerr-soliton pulses in optical fibers are particularly well known [17, 50], and have been considered as a candidate for fiber-optic communications protocols [51, 52]. Microresonators support so-called dissipative cavity solitons, which are localized pulses circulating the resonator that are out-coupled once per round trip. In the case of a single circulating soliton, this leads to a train of pulses propagating away from the resonator with repetition rate  $1/T_{RT}$ . Thus the mode spacing of the comb matches the FSR of the resonator, in contrast with widely-spaced primary comb spectra, and the soliton can, in principle, remain stable and propagate indefinitely as a stationary solution to the LLE. This makes Kerr combs based on solitons particularly attractive for applications.

### 1.3.3.1 Mathematical description of solitons

Solitons in optical fibers are solutions of the nonlinear Schrodinger equation (NLSE) that describes pulse-propagation in optical fiber [17]:

$$\frac{\partial A}{\partial z} = i\gamma|A|^2 A - i \frac{k''}{2} \frac{\partial^2 A}{\partial T^2}. \quad (1.25)$$

This equation describes the evolution of the pulse envelope  $A$  in the ‘fast-time’ reference frame parametrized by  $T$  as it propagates down the length of the fiber, parametrized by the distance variable  $z$ . Here  $\gamma = \frac{2\pi}{\lambda} \frac{n_2}{A_{eff}}$  is the nonlinear coefficient of the fiber, where  $n_2$  is the Kerr index,  $A_{eff}$  is the effective nonlinear mode area and  $\lambda$  is the carrier wavelength, and  $k'' < 0$  is the GVD parameter. The LLE can be viewed as an NLSE with additional loss and detuning terms  $-(1+i\alpha)\psi$  and a driving term  $F$ .

The fundamental soliton solution to the NLSE is:

$$A_{sol} = \sqrt{P_0} \operatorname{sech}(T/\tau) e^{i\gamma P_0 z/2 + i\phi_0}, \quad (1.26)$$

where  $P_0$  is the peak power of the pulse and is related to the duration of the pulse  $\tau$  via  $\tau = \sqrt{-l''/\gamma P_0}$ , and  $\phi_0$  is an arbitrary phase. Thus, this equation admits a *continuum* of pulsed fundamental ‘soliton’ solutions, with one existing for each value of the peak power. Each of these solutions propagates down the fiber without changing shape; only the phase evolves with distance as  $\phi(z) = \gamma P_0 z/2 + \phi_0$ .

The introduction of the loss, detuning, and driving terms into the NLSE to obtain the LLE has several important consequences for solitons. First, exact analytical expressions for the soliton solution to the LLE in terms of elementary functions are not known, in contrast with the situation for the NLSE. However, the soliton solutions to the LLE, Eq. 1.12, can be approximated well as:

$$\psi_{sol} = \psi_{CW,min} + e^{i\phi_0} \sqrt{2\alpha} \operatorname{sech} \sqrt{\frac{2\alpha}{-\beta_2}} \theta. \quad (1.27)$$

Here  $\psi_{CW,min}$  is the flat solution to the LLE from Eq. 1.20 at the point where the soliton solution is desired; when multiple flat solutions exist,  $\psi_{CW,min}$  is the one corresponding to the smallest intensity  $\rho_1$ . The phase  $\phi_0 = \cos^{-1}(\sqrt{8\alpha}/\pi F)$  arises from the intensity-dependent phase shift in the cavity due to the Kerr effect, mathematically described by the term  $i|\psi|^2\psi$ . We depict this approximation, alongside numerical calculations of exact soliton solutions to the LLE, in Fig. 1.7.

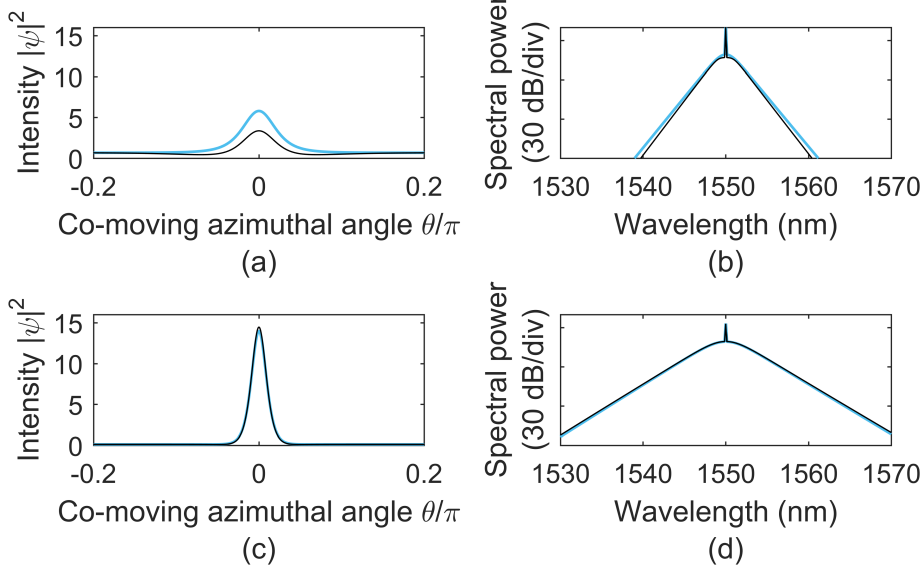


**Figure 1.7: Soliton solutions to the LLE.** Analytical approximations (color) and numerically-calculated exact solutions (black) to the LLE in the time (a,c) and frequency (b,d) domains. The solitons are calculated at  $\alpha = 0.95 \alpha_{max} = 0.95 \pi^2 F^2 / 8$  for  $F^2 = 8\sqrt{3}/9$  (a,b) and  $F^2 = 6$  (c,d) with  $\beta_2 = -0.02$  in both cases. The isolated spectral spike is at the pump frequency and corresponds to the CW background  $\psi_{CW,min}$ . Spectra are calculated using  $f_{rep} = 16.5$  GHz with pump wavelength of  $\lambda_p = 1550$  nm. For experimental measurements of solitons in microring resonators, see Chapters ?? and ??.

This approximation  $\psi_{sol}$  from Eq. 1.27 for the soliton solution of the LLE illustrates a second important consequence of the differences between the NLSE and the LLE: while the NLSE admits a

continuum of fundamental soliton solutions parametrized by their peak power  $P_0$  and arbitrary phase  $\phi_0$ , the LLE supports only one shape for the envelope of a soliton for fixed experimental parameters. Intuitively, this can be understood as arising from the need for the round-trip phase shift for all points on the soliton to be zero in steady-state; the introduction of the detuning parameter  $\alpha$  breaks the degeneracy that exists for the NLSE within the continuum of soliton solutions.

The analytical approximation in Eq. 1.27 indicates the scaling of the amplitude and width of the LLE soliton with the experimental parameters: the amplitude of the LLE soliton, prior to its summation with the CW background, depends only on the detuning  $\alpha$ , and the width of the soliton increases with larger detuning  $\alpha$  and smaller dispersion  $\beta_2$ . Importantly, if one is concerned with maximizing the bandwidth of the soliton, it is important to minimize  $\beta_2$  and maximize  $\alpha$ , due to the inverse relationship between temporal duration and spectral bandwidth. The spectrum of a single-soliton Kerr comb has a  $\text{sech}^2((\omega - \omega_p)/\Delta\omega_{sol})$  envelope, where  $\omega$  is the optical angular frequency and  $\Delta\omega_{sol} \approx \sqrt{32\alpha/|\beta_2|T_{RT}^2}$  is the bandwidth of the pulse in angular frequency. Equivalently, the bandwidth of the soliton in (linear) optical frequency is  $\sqrt{\frac{16\Delta\nu f_{rep}^2}{D_2}\alpha}$ , where  $\Delta\nu$  is the resonance linewidth in linear frequency; the spectral width in mode number is  $\Delta\mu_{sol} \approx 4\sqrt{\alpha\Delta\nu/D_2}$ . Consistent with the phase  $\phi_0$  in the approximation  $\psi_{sol}$  in Eq. 1.27, solitons can exist up to a maximum detuning of  $\alpha_{max} \sim \pi^2 F^2/8$  [31]. For a soliton at the maximum detuning for fixed normalized pump power  $F^2$ , the bandwidth is then  $\sqrt{\frac{\pi^2 \Delta\nu f_{rep}^2}{2D_2} F^2}$ .

Solitons exist only where there is a stable flat solution  $\psi_{CW}$  that is effectively red detuned that can form the background for the pulse [40, 53]. This effectively red-detuned background is itself thermally unstable (see Sec. 1.1.2), but the existence of the soliton acts to stabilize the pump detuning. As explained by Herr et al., the soliton provides a local modulation of the refractive index through the Kerr effect, which changes the round-trip phase shift of pump light that arrives coincidentally with the soliton at the coupling port [31]. This leads to a *local* increase in the resonant wavelength for this pump light. Thus there are effectively two resonant wavelengths, a smaller one determined by the round-trip phase shift including the Kerr shift from the CW background, and a larger one determined by the round-trip phase shift including the Kerr shift from the soliton [54]. The pump laser can be effectively blue-detuned with respect to the latter resonance, which can lead to thermally stable operation in the soliton regime.

Solitons are strongly localized: as can be seen from Eq. 1.27, the deviation of the background intensity from  $\rho_1$  near a soliton at  $\theta_0$  is proportional to  $e^{-(\theta-\theta_0)/\delta\theta}$ , where  $\delta\theta = \sqrt{-\beta_2/2\alpha}$ . If  $\delta\theta$  is sufficiently small, multiple solitons can be supported in the resonator domain  $-\pi \leq \theta \leq \pi$  with very weak interactions between solitons. If the separation between solitons  $i$  and  $j$  at  $\theta_i$  and  $\theta_j$  is small relative to  $\delta\theta$ , the solitons will interact. The topic of soliton interactions is complicated in general, with different types of interactions in different systems (see e.g. Refs. [55–58]). Simulations reveal that if  $(\theta_i - \theta_j)/\delta\theta$  is too small, LLE solitons exhibit attractive interactions as a result of the monotonic (as opposed to oscillatory) decay of the localized pulse to  $\psi_{CW}$  [59], which precludes the existence of stable equilibrium separations. The result of this attraction can be pair-wise annihilation or merger, with the ultimate result being an ensemble with fewer solitons. The maximum number of solitons that can coexist in a resonator in the absence of higher-order stabilizing effects (see Chapter ?? and Refs. [59, 60]) can be approximated as  $N_{max} \approx \sqrt{-2/\beta_2}$  [31]. An approximation to the form of a soliton ensemble is possible as:

$$\psi_{ens} = \psi_{CW,min} + e^{i\phi_0} \sqrt{2\alpha} \sum_j \text{sech} \left( \sqrt{\frac{2\alpha}{-\beta_2}} (\theta - \theta_j) \right), \quad (1.28)$$

where  $\{\theta_j\}$  define the positions of the solitons in the ensemble and  $\phi_0 = \cos^{-1}(\sqrt{8\alpha}/\pi F)$  as above. Fig. 1.8 provides an example illustrating the degeneracy in soliton number of Kerr-combs operating in the soliton regime.

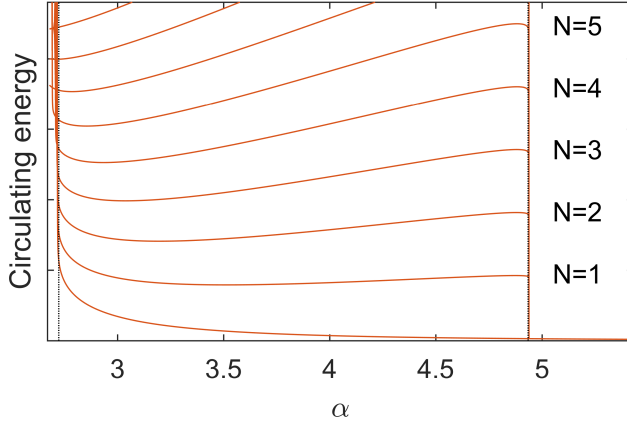


Figure 1.8: **Kerr-soliton energy-level diagram.** Some of the possible values of the circulating energy (proportional to  $\int d\theta |\psi|^2$ ) in the soliton regime as a function of the detuning parameter  $\alpha$ . Level curves correspond to the number of circulating solitons. This diagram is obtained from numerical solutions using  $F^2 = 4$ ,  $\beta_2 = -0.0187$ , and is quantitatively dependent on both of these parameters. Dotted vertical lines indicate approximations to the minimum and maximum detunings for solitons. The approximation for the minimum detuning is the value of  $\alpha$  at which the effectively red-detuned branch vanishes, obtained by inserting  $\rho_-$  (Eq. 1.19) into Eq. 1.17 for  $F^2 = 4$  and solving for  $\alpha$ , and the approximate maximum detuning is  $\alpha_{max} = \pi^2 F^2 / 8$ .

### 1.3.3.2 Microresonator solitons in experiments

Relative to the generation of extended modulation-instability patterns, experimental generation of solitons in microring resonators is challenging. Solitons are localized excitations below threshold, which means that their existence is degenerate with their absence—a resonator can host  $N = 0, 1, 2, \dots$  up to  $N_{max}$  solitons for a given set of parameters  $\alpha$  and  $F^2$ ; as discussed above and illustrated in Fig. 1.8. If  $\alpha$  and  $F^2$  are experimentally tuned to a point at which solitons may exist,  $\psi$  will evolve to a form determined by the initial conditions of the field  $\psi_0$ . To provide initial conditions that evolve to  $N > 0$  solitons, most experimental demonstrations of soliton generation have involved first generating an extended pattern in the resonator, and then tuning to an appropriate point  $(\alpha, F^2)$  so that ‘condensation’ of solitons from the extended pattern occurs.

Condensation of solitons from an extended pattern presents additional challenges. First, it is difficult to control the number of solitons that emerge, due to the high degree of soliton-number degeneracy as shown in Fig. 1.8. This typically leads to a success rate somewhat lower than 100 % in the generation of single solitons. Second, the transition from a high duty-cycle extended pattern to a lower duty-cycle ensemble of one or several solitons comes with a dramatic drop in intracavity power that occurs on the timescale of the photon lifetime. If the resonator is in thermal steady-state before this drop occurs, the resonator will cool and the resonance frequency will increase. If this increase is large enough that the final detuning  $\alpha$  exceeds  $\alpha_{max} = \pi^2 F^2 / 8$ , the soliton is lost. This challenge can be addressed by preparing initial conditions for soliton generation and then tuning to an appropriate point  $(\alpha, F^2)$  faster than the cavity can come into thermal steady-state at the temperature determined by the larger power of the extended pattern; this is possible because the timescale over which an extended pattern can be generated is related to the photon lifetime, which is typically much faster than the thermal timescale.

The first report of soliton generation in microresonators came in 2012 in a paper by Herr et al. [31] (2012 pre-print [30]). These authors described optimizing the speed of a decreasing-frequency scan of the pump laser across the cavity resonance so that solitons could be condensed

from an extended pattern and the scan could then be halted at a laser frequency where the solitons could be maintained with the system in thermal steady-state at the temperature determined by the circulating power of the solitons. Stochastic reduction in the number of solitons in the resonator after condensation from an extended pattern was identified in these experiments. This corresponds to transitions between levels in the diagram in Fig. 1.8, and is associated with discrete steps in a measurement of the ‘comb power,’ the output power of the resonator with the pump frequency  $\nu_p$  filtered out. The resulting staircase-like nature of a comb power measurement is a useful experimental signature of soliton generation in microresonators, and is important for comparison with the results described in Chapter ??.

Other approaches for dealing with the challenges described above have been developed since this first demonstration; these include fast manipulation of the pump power [7, 61] or frequency [62], periodic modulation of the pump laser’s phase or power at  $f_{FSR}$  [14, 63], tuning of the cavity resonance frequency using chip-integrated heaters instead of tuning the pump-laser frequency [64, 65], and soliton-ensemble preparation and subsequent population reduction through manipulation of the pump laser [54]. These methods continue to make use of extended patterns to provide initial conditions for soliton generation. In formally-equivalent fiber-ring resonators, direct generation of solitons without condensation from an extended pattern has been demonstrated using transient phase and/or amplitude modulation of the pump laser [66–68].

### 1.3.3.3 Microresonator solitons in applications

Because solitons have single-FSR spacing, have the output localized into a high peak-power pulse, and are stationary (in contrast with chaos, which has single-FSR spacing but is not stationary), they are promising for applications. Many of the proposals for and demonstrations of applications with Kerr-combs have used single-soliton operation. Some of the applications already demonstrated include an optical clock [69], dual-comb spectroscopy [70], coherent communications [71], and direct on-chip optical frequency synthesis [72]. Additionally, soliton combs have been self-referenced both with [73, 74] and without [75, 76] external spectral broadening. Nevertheless, there remains work to be done to bring microresonator-soliton technology to the level of maturity that will be required for deployment in the field. Chapters ?? and ?? describe two recent advancements: the development of a method for direct on-demand generation of single solitons by use of a phase-modulated pump laser, and the observation and explanation of a soliton-interaction mechanism that imparts rigid structure on the allowed configurations of multi-soliton ensembles.

## Chapter 2

### Theory of Kerr frequency combs in Fabry-Perot resonators

Generation of Kerr frequency combs in the ring-resonator geometry appears quite promising for applications. However, a second possibility is to use the same processes for comb generation, but with a Fabry-Perot (FP) resonator geometry. The FP geometry offers a new degree of freedom relative to the ring resonator, which is the possibility to employ chirped mirrors, mirror coatings, or distributed Bragg reflectors, and therefore exert greater control over the total cavity dispersion. Other differences with the ring geometry may ultimately prove important, for example the smaller footprint possible in a cavity of total length  $L$  with the FP geometry versus the ring geometry could allow for denser and more flexible integration of Kerr combs in photonics systems. Kerr-comb generation in an FP cavity was reported in 2009 Ref. [13] and soliton generation using a pulsed pump laser was recently described in Ref. [14].

In this chapter we present a brief theoretical investigation of the difference in the nonlinear dynamics that occur in a Kerr-nonlinear FP resonator versus a Kerr-nonlinear ring resonator. Our starting point is the Fabry-Perot Lugiato-Lefever equation (FP-LLE), which is derived in detail in Ref. [Cole2018a], beginning from a set of coupled equations that describe the interaction of the envelopes for the forward- and backward-propagating fields in the cavity with the Kerr medium. A derivation of equivalent coupled mode equations is provided in Ref. [14]. We do not reproduce the derivation of the equation here; our goal is to understand its description of Kerr-comb dynamics. The equation is:

$$\frac{\partial \psi}{\partial \tau} = -(1 + i\alpha)\psi + i|\psi|^2\psi - i\frac{\beta_2}{2}\frac{\partial^2 \psi}{\partial \theta^2} + 2i\psi \langle |\psi|^2 \rangle + F. \quad (2.1)$$

Here,  $\langle g \rangle$  denotes the spatial average over the domain:  $\langle g \rangle = \frac{1}{2\pi} \int_{-\pi}^{\pi} d\theta g(\theta)$ . This equation is identical to the LLE for the ring cavity except for the term  $2i\psi \langle |\psi|^2 \rangle$  describing modulation by twice the average of the intracavity power. The coordinate  $\theta$  is defined as  $\theta = 2\pi z/2L$ , where  $z$  is a co-moving longitudinal coordinate (so that, for example, solitons are stationary functions of  $\theta$ ) on a domain  $-L \leq z \leq L$ ;  $L$  is the physical length of the Fabry-Perot cavity. The time  $\tau$  is once again normalized to twice the photon lifetime  $\tau_\gamma$ :  $\tau = t/2\tau_\gamma$ . The normalized experimental parameters in the FP-LLE are the same as in the LLE for the ring cavity, with  $\alpha$  the detuning,  $\beta_2$  the dispersion, and  $F^2$  the pump power:

$$\alpha = -\frac{2(\omega_o - \omega_c)}{\Delta\omega_o}, \quad (2.2)$$

$$\beta_2 = -\frac{2D_2}{\Delta\omega_{tot}} = -\frac{2}{\Delta\omega_o} \frac{\partial^2 \omega_\mu}{\partial \mu^2} \Big|_{\mu=0}, \quad (2.3)$$

$$F^2 = \frac{8g_o \Delta\omega_{ext}}{\Delta\omega_{tot}^3} \frac{A_{eff}}{A_{in}} \frac{n_o}{n_{ext}} \frac{P}{\hbar\omega_o}. \quad (2.4)$$

In the above,  $\omega_\mu$  represents the set of resonance frequencies of the cavity including the effects of dispersion, with  $\mu = 0$  indexing the pumped mode (see e.g. Ref. [61]). The cavity loss and coupling rates  $\Delta\omega_{tot}$  and  $\Delta\omega_{ext}$  are related to the mirror reflectivity  $R$  and transmission  $T$  via  $\Delta\omega_{tot} = (1 - R)c/n_g L$  (where two identical mirrors are assumed) and  $\Delta\omega_{ext} = cT/2n_g L$ , with

$n_g = c/v_g$  the group index. The quantities  $A_{in}$  and  $A_{eff}$  represent the mode's effective area  $\pi w_{in}^2$  (for a Gaussian mode of radius  $w$ ) at the input mirror and the same averaged over the cavity of length  $L$ ,  $\frac{\pi}{L} \int dz w(z)^2$ , respectively. Further,  $g_o = n_2 \hbar \omega_o^2 D_1 / (2\pi n_g A_{eff})$  is the nonlinear gain parameter, where  $D_1 = \left. \frac{\partial \omega_\mu}{\partial \mu} \right|_{\mu=0}$  is the cavity free-spectral range in angular frequency (here and in Eq. (2.3)  $\mu$  is treated as a continuous variable). The nonlinear index  $n_2$  is related to the third-order susceptibility via  $\chi^{(3)} = (4/3)n_o^2\epsilon_o c n_2$ , where  $n_o$  is the refractive index of the nonlinear medium. The power  $P = \eta P_{inc}$  denotes the mode-matched power, with mode-matching factor  $\eta$  and power  $P_{inc}$  incident on the input mirror, and  $n_{ext}$  is the refractive index of the medium external to the cavity.

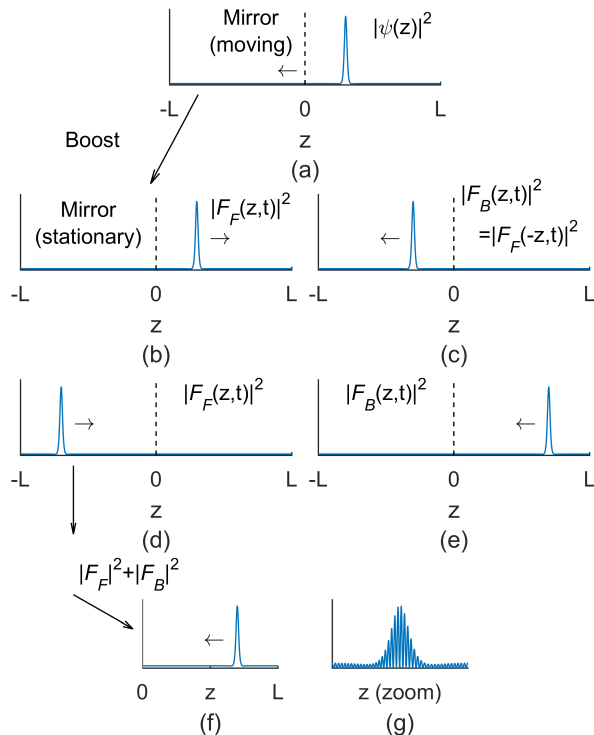


Figure 2.1: **Relationship between the physical field in the Fabry-Perot cavity and the co-moving field  $\psi$ .** (a) A soliton stationary solution to the FP-LLE in the co-moving domain of length  $2L$ , in which the physical components of the cavity (e.g. mirror) move. (b) Intensity of the field  $F_F$  in the lab frame, in which the cavity is stationary. (c) Intensity of  $F_B$  in the lab frame, related to  $F_F$  by reflection about the origin. (d,e) Depictions of the same after propagation for half of the cavity round-trip time. (f) Total intensity of the field on the physical domain  $0 \leq z \leq L$ . (g) The intensity of the field including the background standing wave that results multiplication of  $F_F$  and  $F_B$  by the appropriate traveling waves.

The formulation of the FP-LLE in terms of the field  $\psi$  defined in the co-moving domain of length  $2L$  facilitates numerical simulation of the nonlinear dynamics. To obtain the physical, propagating field in the Fabry-Perot cavity, the arguments of the field  $\psi$  are transformed back to dimensionful parameters so that we have  $\psi(z, t)$ , and then it is boosted to group velocity  $v_g$  in the domain of length  $2L$  to obtain  $\bar{\psi}$ , which propagates with periodic boundary conditions  $\bar{\psi}(-L, t) = \bar{\psi}(L, t)$ . From  $\bar{\psi}(z, t)$  we define functions  $F_F$  and  $F_B$  that are proportional to the forward-propagating and backward-propagating envelopes of the electric field as  $F_F(z, t) \propto \bar{\psi}(z, t)$  and  $F_B(z, t) \propto \bar{\psi}(-z, t)$ , so that they are related by reflection about  $z = 0$ . The quantity  $|F_B(z, t)|^2 + |F_F(z, t)|^2$  on the

physical domain  $0 \leq z \leq L$  is then proportional to the intensity in the FP cavity as a function of time, averaged over fast spatial and temporal oscillations associated with the optical frequency. If desired, these can be included by multiplying  $F_B$  and  $F_F$  by the appropriate traveling waves before summation. This process is depicted schematically in Fig. 2.1.

In the remainder of this chapter we provide an investigation of the nonlinear dynamics in a Fabry-Perot cavity as they relate to the generation of frequency combs. We will focus here exclusively on the properties of FP solitons, as these have been identified as the most promising route towards meeting application needs with Kerr-combs.

## 2.1 General relationship between the ring LLE and the FP-LLE

As can be seen from Eq. 2.1 for the Fabry-Perot cavity and Eq. 1.12 for the ring cavity, the difference between the two geometries lies in the term in the FP-LLE  $2i\psi \langle |\psi|^2 \rangle$ . This term represents the cross-phase modulation of the field  $\psi(\theta, \tau)$  at each co-moving point  $\theta$  by each other co-moving point  $\theta'$  as  $\theta$  and  $\theta'$  propagate through each other during a round trip of the Fabry Perot cavity. The incorporation of this effect into the FP-LLE as a spatial average is consistent with the inclusion of the drive  $F$  and out-coupling  $\Delta\omega_{ext}$  (which is included in the damping term  $\partial\psi/\partial\tau = -\psi$ ) into the LLE as delocalized, constant operators; this approximation is valid for high-finesse cavities, in which the field  $\psi$  changes little on the timescale of a round trip.

We can investigate the stationary solutions to the FP-LLE by setting the time derivative to zero, and we find:

$$0 = -(1 + i\alpha)\psi + i|\psi|^2\psi + 2i\psi \langle |\psi|^2 \rangle - i\frac{\beta_2}{2} \frac{\partial^2\psi}{\partial\theta^2} + F \quad (2.5)$$

$$= -(1 + i(\alpha - 2\psi \langle |\psi|^2 \rangle))\psi + i|\psi|^2\psi - i\frac{\beta_2}{2} \frac{\partial^2\psi}{\partial\theta^2} + F \quad (2.6)$$

$$= -(1 + i\alpha')\psi + i|\psi|^2\psi - i\frac{\beta_2}{2} \frac{\partial^2\psi}{\partial\theta^2} + F, \quad (2.7)$$

where we have defined  $\alpha' = \alpha - 2 \langle |\psi|^2 \rangle$ . We can immediately see from Eq. 2.7 that the stationary solutions to the FP-LLE at a point  $(\alpha, F^2)$  are the same as the stationary solutions to the ring LLE at the point  $(\alpha', F^2)$ . Physically, this arises from the need for increased detuning to compensate for the increased Kerr phase-shift due to cross-phase modulation by the full waveform so that the round-trip phase shift is maintained at zero for each point  $\theta$  in the co-moving frame. As a consequence of this relationship, we expect that the FP-LLE exhibits the same stationary solutions as the ring LLE: Turing patterns and solitons. In the remainder of this chapter we briefly discuss extended patterns (Turing patterns and chaos) in the FP-LLE, and then provide a longer discussion of solitons in the FP-LLE and how they differ from solitons in the ring geometry.

## 2.2 Extended patterns in the FP-LLE

We confirm the existence of Turing patterns and spatiotemporal chaos under the FP-LLE with numerical simulations of Eq. 2.1. A Turing pattern simulated at the point  $(\alpha = 2.5, F^2 = 6)$  is plotted in the  $\theta$  domain in Fig. 2.2. An interesting contrast between the ring and FP geometries lies in the nature of stationary solutions to Eq. 2.1. For a stationary solution to the ring LLE, the intensity profile remains constant up to simple circulation about the ring at the group velocity. This is not the case for the FP-LLE, where a stationary solution to 2.1 such that  $\partial\psi/\partial\tau = 0$  does not correspond to a time-invariant intensity pattern, due to the intensity interference between counter-propagating components of  $\psi$ . We demonstrate this by plotting in Fig. 2.2b the physical intensity pattern (averaged over fast spatial and temporal oscillations) in the FP cavity corresponding to the Turing pattern shown in Fig. 2.2a at two different times. As the fields  $F_F$  and  $F_B$  circulate in the cavity, the number and positions of intensity maxima change.

The FP-LLE also exhibits chaos. In Fig. 2.2c we plot a snapshot of a chaotic waveform simulated at the point  $(\alpha = 5.3, F^2 = 8)$ . It is interesting to note that as  $\psi$  varies in time so

does the average intensity  $\langle |\psi|^2 \rangle$ . This leads to a time-varying effective detuning value  $\alpha' = \alpha - 2\langle |\psi|^2 \rangle$ . A natural question, then, is whether this time-varying  $\alpha'$  effects the dynamics of chaos. We investigate this by conducting a simulation of chaos with a duration of 10,000 photon lifetimes under the FP-LLE at the point  $(\alpha = 5.3, F^2 = 8)$ . We then calculate the time-averaged  $\alpha'$  value:  $\overline{\alpha'} = \alpha - 2\langle |\psi|^2 \rangle = 1.1$ , and conduct a ring-LLE simulation at the corresponding point. To compare the dynamics of chaos in each case, we record the amplitudes of local maxima in  $|\psi|^2$  throughout the simulation. This data is displayed in histograms in Fig. 2.2d, from which it is apparent that this calculation does not reveal a significant difference between the chaotic dynamics in ring resonator and FP cavities. Nevertheless, this could be an interesting subject to investigate further.

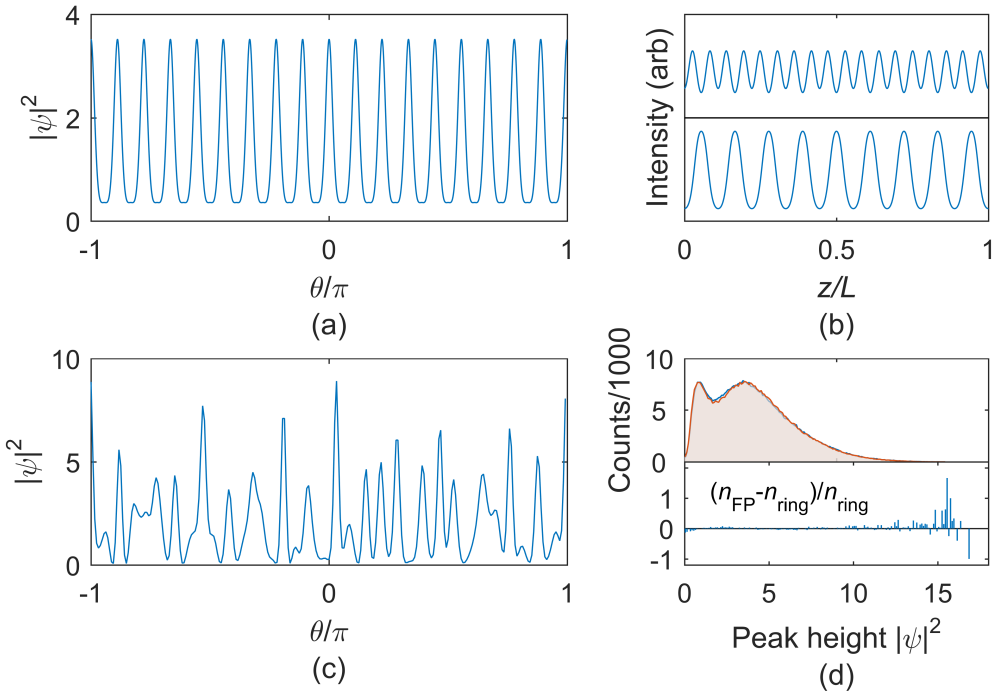


Figure 2.2:

## 2.3 Solitons in the FP-LLE

### 2.3.1 Analytical approximation for solitons in the FP-LLE

Equipped with the definition  $\alpha' = \alpha - 2\langle |\psi|^2 \rangle$  and the relation given in Eq. 2.7, we can investigate the soliton solutions to the FP-LLE. We can immediately adapt the analytical approximation to the soliton solution for the ring LLE, which we recall here for convenience, indicating parameters defined by the detuning for the ring LLE with the ‘prime’ superscript as in  $\alpha'$ :

$$\psi_{sol} = \psi'_{s,min} + e^{i\phi'_0} \sqrt{2\alpha'} \operatorname{sech} \sqrt{\frac{2\alpha'}{-\beta_2}} \theta. \quad (2.8)$$

Here  $\psi'_{s,min}$  is the flat solution to the ring LLE from Eq. 1.20 at the point where the soliton solution is desired; when multiple flat solutions exist,  $\psi'_{s,min}$  is the one corresponding to the smallest intensity  $\rho'_1$  found by solving  $F^2 = (1 + (\alpha' - \rho')^2)\rho'$ . The phase  $\phi'_0$  is again defined as  $\phi'_0 = \cos^{-1}(\sqrt{8\alpha'}/\pi F)$ .

Thus, an approximate soliton solution to the ring LLE according to Eq. 2.8 is also an approximate soliton solution to the FP-LLE at the detuning  $\alpha$ , where:

$$\alpha = \alpha' + \frac{1}{\pi} \int d\theta |\psi_{sol}|^2 \quad (2.9)$$

$$\begin{aligned} &= \alpha' + 2\rho'_1 + \frac{2}{\pi} \sqrt{-2\alpha'\beta_2} \tanh \left( \pi \sqrt{\frac{2\alpha'}{-\beta_2}} \right) \\ &\quad + \frac{8}{\pi} \sqrt{-\beta_2\rho'_1} \cos(\phi' - \phi'_0) \tan^{-1} \tanh \left( \pi \sqrt{\frac{\alpha'}{-2\beta_2}} \right) \end{aligned} \quad (2.10)$$

and  $\phi' = \tan^{-1}(\rho'_1 - \alpha')$ . To find the approximate soliton solution to the FP-LLE at a point  $(\alpha, F^2)$ , Eq. 2.10 must be numerically inverted to find  $\alpha'$ , after which  $\psi_{sol}$  can be obtained. As for the ring LLE, an approximation to multi-soliton ensembles is possible as:

$$\psi_{ens} = \psi'_{s,min} + \sqrt{2\alpha'} e^{i\phi'_0} \sum_j \operatorname{sech} \left( \sqrt{\frac{2\alpha'}{-\beta_2}} (\theta - \theta_j) \right). \quad (2.11)$$

Such an ensemble may or may not be stable, depending on the separation between the locations of the solitons  $\{\theta_j\}$  and the temporal width of the solitons determined by  $\alpha'$  and  $\beta_2$ . Each soliton in the ensemble contributes to the average intensity  $\langle |\psi|^2 \rangle$ , so Eq. 2.10 no longer holds; instead, Eq. 2.11 must be integrated to determine a new value for  $\alpha'$ .

### 2.3.2 Existence range of single solitons

An important consequence of the additional nonlinear term  $2i\psi \langle |\psi|^2 \rangle$  in the FP-LLE is that the range of parameters over which single solitons exist acquires a dependence on the dispersion parameter  $\beta_2$ , through the effect of dispersion on pulse energy. This is in contrast to the situation for the ring LLE, where the existence range is independent of  $\beta_2$ . For the FP-LLE the existence range also depends on the number of co-propagating pulses and can be greatly extended in the case of many co-propagating solitons; we don't discuss that at length here.

The minimum value of detuning  $\alpha$  at which solitons exist as a function of  $F^2$  is determined by the existence of a stable flat solution to the LLE that can form the c.w. background for the soliton. The maximum value of detuning for which solitons can exist is determined by  $\alpha' = \alpha - 2\langle |\psi|^2 \rangle$  according to  $\alpha'_{max}(F^2) = \pi^2 F^2 / 8$ , which approximately gives the maximum detuning for solitons in the ring LLE [31].

For the FP-LLE, a stable flat solution exists to the right of the line  $F_+^2(\alpha)$  in the  $\alpha - F^2$  plane that bounds from above the region of multiple flat solutions. As we did for the ring LLE, we calculate this line by beginning from the equation describing intensity of the flat stationary solutions  $\rho$  to the FP-LLE:

$$F^2 = (1 + (\alpha - 3\rho)^2)\rho. \quad (2.12)$$

There are multiple flat solutions between the values  $\rho_\pm$  at which  $\partial F^2 / \partial \rho = 0$ ; the upper boundary of this region  $F_+^2(\alpha)$  is obtained by inserting  $\rho_- = (2\alpha - \sqrt{\alpha^2 - 3})/9$  into Eq. 2.12:

$$F_+^2(\alpha) = \left[ 1 + \left( \frac{\alpha + \sqrt{\alpha^2 - 3}}{3} \right)^2 \right] \frac{2\alpha - \sqrt{\alpha^2 - 3}}{9} \quad (2.13)$$

This curve bounds the region of soliton existence on the left (lower  $\alpha$ ) in the limit  $\beta_2 \rightarrow 0^-$  ( $\beta_2$  goes to zero from below). In the same limit, the right boundary of soliton existence (higher  $\alpha$ ) is the line  $\alpha_{max}(F^2) = \alpha'_{max}(F^2) + 2\rho'_1(\alpha'_{max}(F^2), F^2)$ , where  $\rho'_1(\alpha', F^2)$  is the intensity of the smallest flat solution to the ring LLE at  $(\alpha', F^2)$ .

We can obtain approximations to the bounds of soliton existence for finite  $\beta_2$  by first finding the amplitudes  $\rho_L(F^2)$  and  $\rho_R(F^2)$  of the soliton background for the left and right boundaries of soliton existence in the zero-dispersion limit and then using Eq. 2.10 to calculate the value of  $\alpha$  at which a soliton exists on a background of that amplitude for finite  $\beta_2$ . These results are summarized in Fig. 2.3. Fig. 2.3a shows the curves corresponding to the  $\beta_2 \rightarrow 0^-$  limit and for finite  $\beta_2$  values of -0.001, -0.02, and -0.3, and Fig. 2.3b shows a comparison between the approximate curves for finite  $\beta_2$  and the soliton existence boundaries as revealed by full simulations of the FP-LLE. The analytical approximation is accurate for low  $F^2$  and small dispersion, but becomes less accurate as these quantities increase. This is because breather solitons whose amplitudes oscillate periodically are found near  $\alpha_{min}$  for larger values of  $F^2$ . Breather solitons are accompanied by traveling waves that propagate away from the soliton and diminish in amplitude as they do so, and their range increases with the dispersion. For larger values of dispersion these waves fill the cavity, and in this case the flat background whose stability forms the basis for approximating the dispersion-dependent boundary curves is actually not present.

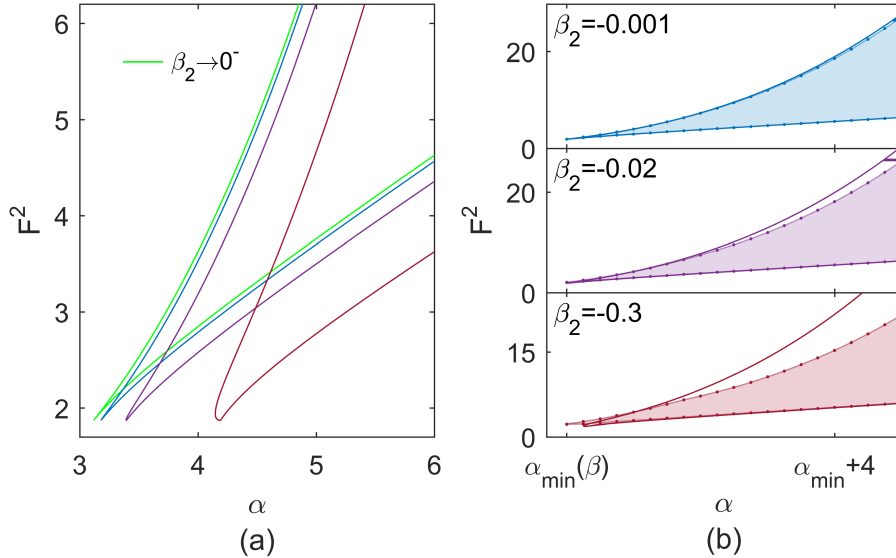


**Figure 2.3: Boundaries of soliton existence in the FP-LLE.** (a) Exact boundary of soliton existence for the limit  $\beta_2 \rightarrow 0^-$  and analytical approximations to the boundaries for three finite values of dispersion:  $\beta_2 = -0.001$  (blue),  $\beta_2 = -0.02$  (purple), and  $\beta_2 = -0.03$  (red). (b) Comparison between the finite-dispersion approximations from (a) and soliton existence boundaries as revealed by full simulations of the FP-LLE.

The lines  $\alpha_{min}(F^2)$  and  $\alpha_{max}(F^2)$  intersect at  $F^2 = F_I^2 \approx 1.87$ . Below this value of the pump power solitons do not exist for the FP-LLE, and this can be seen as follows: The value of  $\rho'_{min}$  describing the amplitude of the soliton background along the line of maximum detuning  $\alpha'_{max}$  for the ring LLE is in general also a flat solution  $\rho$  of the FP-LLE at the corresponding point  $\alpha_{max} = \alpha'_{max} + 2\rho'_{min}(\alpha'_{max}, F^2)$ . However, when  $F^2 < F_I^2 \approx 1.87$ , the flat solution  $\rho'_{min}$  to the ring LLE is not the smallest flat solution to the FP-LLE; instead, it is the middle of three, and is therefore unstable. Therefore, when  $F^2 < F_I^2$  the line  $\alpha_{max}(F^2)$  as defined above does not represent the right boundary of soliton existence for the FP-LLE. In fact, below this point, for all values of  $\alpha$  where a stable flat solution to the FP-LLE  $\rho_{min}$  exists,  $\alpha - 2\rho_{min}(\alpha, F^2) > \alpha'_{max}$ , preventing the existence of solitons. This is an interesting contrast with the ring LLE, where the corresponding lines bounding soliton existence intersect at  $F^2 = 1.175$  and where we can verify in simulations that

solitons exist for e.g.  $F^2 = 1.5$ .

### 2.3.3 Generation of single solitons through laser frequency scans

A second important consequence of the additional nonlinear term in the FP-LLE relative to the ring LLE is an increase in the range of  $\alpha$  values, for a given value of  $F^2$ , at which the state of  $\psi$  can be either an extended pattern (spatiotemporal chaos or Turing pattern) or a soliton/soliton ensemble. This is because the extended patterns fill the domain and, because of their higher average intensity, experience a greater nonlinear shift than lower duty-cycle single solitons or soliton ensembles due to the additional nonlinear term. Here we discuss the implications of this fact for the experimental generation of single solitons through decreasing-frequency scans of the pump laser, as discussed in Chapter 1, Sec. 1.3.3. We summarize the results in Fig. 2.4. In Fig. 2.4a we show example simulations of spatiotemporal chaos and a single soliton to illustrate this degeneracy. Both of these simulations are conducted at the point  $(\alpha = 8, F^2 = 8)$ , and the soliton and chaos are also degenerate with a stable flat solution, with the nature of  $\psi$  dependent upon the initial conditions.

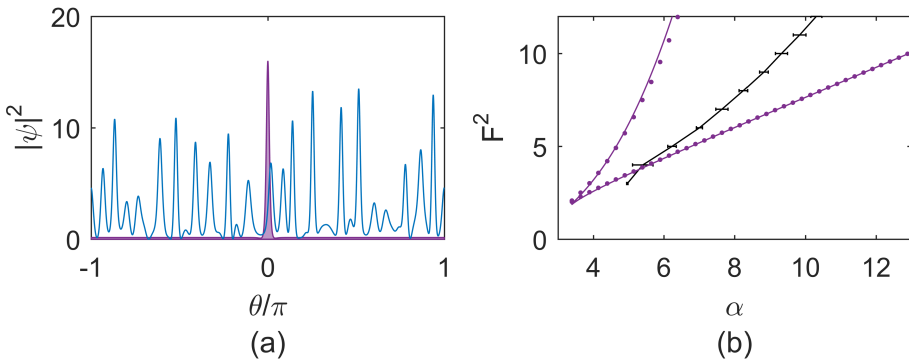


**Figure 2.4: Transition from extended patterns to single solitons in the FP-LLE.** (a) Simulated spatiotemporal chaos (blue) and single soliton solution (purple), either of which can exist at the point  $(\alpha = 8, F^2 = 8)$ . The amplitude of the soliton is larger than the characteristic amplitude of the features in the chaos because the effective detuning  $\alpha'$  is larger for the soliton. (b) Analytical and numerical soliton existence limits (purple) for  $\beta = -0.02$  from panel (a) and the upper bound in  $\alpha$  for the existence of spatiotemporal chaos/Turing patterns (black with error bars), estimated as described in the text.

It has been established that condensation of solitons from an extended pattern in a sweep in which  $\alpha$  increases is a useful way of obtaining single solitons in experiments. Because this method relies on the excitation of an extended pattern (chaos or Turing pattern) to provide initial conditions out of which solitons condense as  $\alpha$  is increased, it is important that the maximum detuning (the value of  $\alpha$  where  $\alpha' = \alpha'_{max} = \pi^2 F^2 / 8$ ) for single solitons is larger than the  $\alpha$  value at which an extended pattern will transition to a soliton ensemble. Otherwise, the generation of single solitons using this method will be difficult or impossible. To investigate this, we numerically perform slow scans across the resonance to identify where the transition from extended patterns to independent solitons occurs. These scans are conducted slowly to approximate adiabaticity:  $d\alpha/d\tau = 2.5 \times 10^{-4}$ . We perform 10 scans across the resonance at each integer value of  $F^2$  from 3 to 12 with  $\beta = -0.02$ , and we identify the transition from extended pattern to independent solitons by inspection of several quantities as  $\alpha$  is varied: the set of local maxima and minima of  $|\psi|^2$  (see [41]), the distance between local maxima, and the number of local maxima above  $|\psi|^2 = 1$ . In Fig. 2.4b we plot the line representing the upper boundary in  $\alpha$  of extended patterns obtained in the scans across the resonance. Error bars represent the standard deviation of the values  $\alpha$  at which the transition is observed, with this spread in the values arising due to the chaotic fluctuations in the total intracavity

power and therefore also in the size of the nonlinear integral term. These results indicate that the region over which single solitons exist and extended patterns do not is narrow for small pump powers  $F^2$ , and widens as  $F^2$  is increased. Without performing experiments, it is impossible to precisely quantify the limitations imposed by this observation, but we expect this finding to be useful in refining schemes for single-soliton generation in Fabry-Perot resonators. It is important to note that challenges associated with the necessary transition from high duty-cycle extended patterns to low duty-cycle solitons are alleviated by pulsed pumping, which was the technique used by Obrzud, Lecomte, and Herr in their recent report of soliton generation in FP resonators.

## Chapter 3

### Microresonator-based frequency combs: Summary and outlook

Chapters 1-2 discussed generation of frequency combs from a continuous-wave laser by parametric frequency conversion in Kerr-nonlinear resonators. I described three results: 1. The investigation and implementation of a technique for spontaneous soliton generation in Kerr resonators using a phase-modulated pump laser, 2. The observation and explanation of soliton crystals in Kerr resonators, and 3. A theoretical investigation of Kerr-comb generation in Fabry-Perot cavities, with an emphasis on the properties of solitons and soliton generation. These results all help to more clearly define what is possible with these systems, and suggest avenues for further research.

Soliton generation with a phase-modulated pump laser is a promising candidate for inclusion in chip-integrated Kerr-comb systems as the mechanism by which single-soliton operation is initiated. Two directions for continued work are additional theoretical investigations of the full LLE with a phase-modulated pump, which could provide insight into the dynamics beyond what is possible using the approximations described in Chapter ??; and implementation of the technique with resonators that have electronically-inaccessible free-spectral ranges, using the subharmonic-modulation approach that was proposed. Incorporation of the technique into a chip-integrated Kerr-soliton comb may also require modification and further development of the technique that was used to overcome thermal instabilities associated with the increasing-frequency pump-laser scan.

The investigation of soliton crystals presented here serves several important purposes. First, it represented an important step towards full explanation of observed Kerr-comb phenomena in terms of the LLE model. Second, soliton crystals have the attractive properties of single-soliton Kerr combs, with the additional property that a soliton crystal of  $N$  pulses has conversion efficiency of pump-laser power into the comb that is roughly  $N$  times higher than a comparable single-soliton comb. With careful preparation of a particular crystal state, this could make them attractive for applications like optical arbitrary waveform generation and nonlinear spectroscopy. Additionally, soliton crystals present a hugely degenerate configuration space that could be useful in implementations, for example, of an on-chip optical buffer or in communications applications [32]. Finally, experimental generation of soliton crystals is significantly simpler than generation of single solitons, where the change in the duty cycle of the optical waveform from extended pattern to single soliton leads to thermal instabilities that are alleviated only with precise control of the pump-laser power and frequency. Thus, it is possible to propose a scheme for deterministic on-chip soliton crystal generation that makes use of two resonators, each constructed of looped single-mode optical waveguides. One resonator is pumped by a laser and hosts the soliton crystal. The second resonator need not be pumped, and exists to provide a specific perturbation to the mode structure of the first resonator to enable soliton crystallization; this could be achieved through careful engineering of the coupling between the resonators. If the free-spectral range of the second resonator is considerably higher than the free-spectral range of the first, and not near one of its harmonics, then realization of single-mode perturbation to the mode structure of the first resonator could be achieved. Implementing deterministic soliton crystal generation on a chip in this way could greatly simplify requirements on the other components in a system for full-integration of Kerr solitons, as soliton generation could be achieved through slow tuning of the pump laser.

The theoretical investigation of Kerr-comb generation in the Fabry-Perot geometry will pro-

am I citing  
pascal in sc  
chapter?

vide useful guidance for future experimental work. An obvious direction for continued work is the generation of solitons in Fabry-Perot cavities that make use of the additional degree of freedom provided by the dispersion applied by reflection at the ends of the cavity. This would build on previous experiments [13, 14]. In fact, soliton generation in Fabry-Perot cavities constructed of potted fiber ferrules with high-reflectivity end-coatings has already been realized at NIST Boulder [**Zhang2018**], but there remains work to be done to achieve control the total cavity dispersion with chirped mirror-coatings. Unresolved questions include the effect of uncontrolled expansion of the mode in the coating on both the mirror reflectivity and its group-velocity dispersions. Looking to the chip scale, integrated Fabry-Perot cavities constructed of single-mode waveguides with photonic-crystal mirrors is a promising route for development that would further reduce the footprint of Kerr-comb systems. This work is ongoing at NIST Boulder, and primary comb has been observed in such a cavity [**Yu2018**]. Finally, I note that the proposal for deterministic chip-scale generation of soliton crystals presented above could be realized with two co-linear on-chip Fabry-Perot cavities, where the first cavity hosts the crystal, which is out-coupled in reflection, and the second cavity provides a perturbation to the first cavity's mode structure.

## Chapter 4

### EOM Combs

In this chapter, I discuss the generation of high-repetition-rate frequency combs through electro-optic modulation of a continuous-wave laser—so-called EOM combs [77–86]. This scheme represents an alternative to parametric generation of high-repetition-rate combs in Kerr resonators, and as the technology matures it will likely find a niche in the application space that leverages its long-term stability, lack of moving parts, and possibility for robust turn-key operation. First I present the operational principle, followed by experimental results that represent the first  $f - 2f$  self-referencing of a comb of this kind. Then I provide a discussion of the noise processes specific to the EOM comb, the investigation and mitigation of which is a significant contribution of the work described here. I conclude with a brief outlook for the technology.

#### 4.1 Principle of operation

At its simplest, an EOM comb is a set of lines generated by passing a CW ‘seed’ laser through cascaded phase and intensity modulators to generate a train of chirped pulses. After this initial step, the pulse train may be propagated through a dispersive medium to temporally compress the pulses, and they can be subsequently spectrally broadened. A generic expression for the electric field before temporal compression results from the product of carrier field  $E_o e^{i\omega_c t}$  with operators

$$\frac{e^{i\Phi(t)} + e^{-i\Phi(t)}}{2} = \cos \Phi(t), \quad (4.1)$$

where

$$\Phi(t) = \phi_{DC} + \phi_{RF} \sin(\omega_{rep}t + \phi_{IMPM}) \quad (4.2)$$

representing the intensity modulation and

$$\exp[i\delta_{PM} \sin \omega_{rep}t] \quad (4.3)$$

representing the phase modulation. Here  $E_o$  and  $\omega_c$  are the complex amplitude and the carrier frequency of the seed laser. The phases  $\phi_{DC}$  and  $\phi_{RF}$  represent the DC bias and depth of the intensity modulation, respectively, which experimentally are sourced from a DC power supply and an RF synthesizer. Writing the intensity-modulation operator as the sum of exponentials reveals the physical origin of intensity modulation as phase modulation in two paths with opposite sign. The phase-modulation index, which sets the initial bandwidth of the EOM comb, is  $\delta_{PM}$ . The comb’s repetition rate is  $f_{rep} = \omega_{rep}/2\pi$ , with  $\omega_{rep}$  the angular frequency of the phase and intensity modulation. In practice it is useful to derive these signals from the same synthesizer. The phase  $\phi_{IMPM}$  represents a phase difference between the IM and PM operators arising from path-length differences, which can be controlled via the insertion of a phase shifter in one electrical path.

For convenient temporal pulse compression and subsequent spectral broadening of the comb it is desirable to configure the IM and PM to yield a train of 50 % duty-cycle pulses with normal chirp (temporally increasing carrier frequency). To achieve this, both  $\phi_{DC}$  and  $\phi_{RF}$  are set to  $\pi/4$  and  $\phi_{IMPM}$  is set to zero. Experimentally, one can determine the appropriate RF drive power and bias by

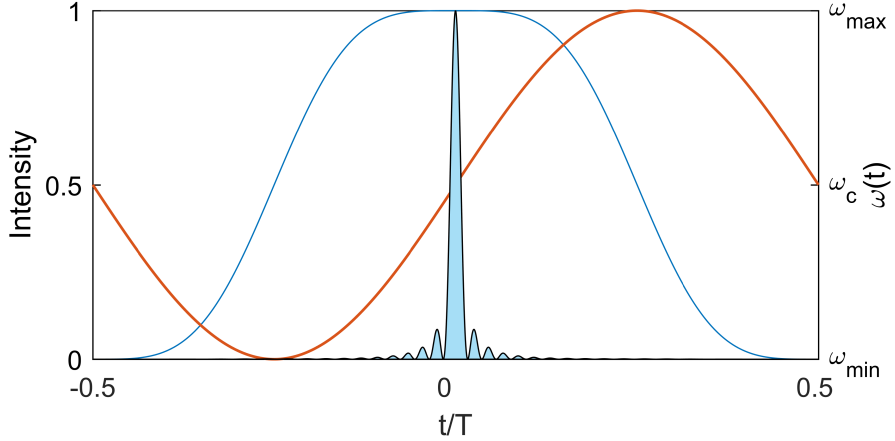


Figure 4.1: **Operating principle of an electro-optic modulation comb.** A train of chirped pulses is generated by combined electro-optic phase and intensity modulation, and the pulses can then be conveniently temporally compressed in a dispersive medium. Light blue line (plotted with respect to the left axis): Initial intensity profile of a single EOM comb pulse as described by Eq. 4.4. Orange (right axis): Instantaneous carrier frequency, which varies about  $\omega_c$  by  $\pm\delta_{PM}\omega_{rep}$  and increases approximately linearly in time while the pulse amplitude is high. Solid blue (left axis): Pulse resulting from compression of the initial pulse to its transform limit. The temporal duration of this pulse decreases as  $\delta_{PM}$  increases as a result of the increased bandwidth of the comb; here the phase-modulation depth  $\delta_{PM} = 31\pi/4$  is used. The compressed pulse has higher peak power (in this case by a factor of 26.5); for convenient depiction of both pulses the compressed pulse has been rescaled.

adjusting the ratios  $\eta_1 = P_1/P_0$  and  $\eta_2 = P_2/P_0$  between the first- and second-order sidebands and the carrier to  $\eta_1 = -7.4$  dB and  $\eta_2 = -21.3$  dB with only intensity modulation applied to the seed laser.<sup>1</sup> Setting  $\phi_{IMPM}$  to either zero or  $\pi$  is achieved by examining the optical spectrum of the EOM comb with both IM and PM applied. The spectrum is asymmetric if  $\phi_{IMPM}$  is not zero or  $\pi$  due to stronger transmission of either the high- or low-frequency components of the phase-modulated seed laser through the intensity modulators. The optical spectrum of the comb, which does not include phase information, is the same for  $\phi_{IMPM} = 0$  or  $\pi$ ; the difference between the two corresponds to reversal of the field in time or, equivalently, the difference between normal and anomalous chirp. Setting  $\phi_{IMPM}$  to zero is accomplished by verifying that the pulses are compressed by propagation in an appropriate length of an anomalously dispersive medium;  $\phi_{IMPM} = \pi$  corresponds to anomalous chirp on the initial pulse train, in which case the pulses will not be compressed.

A simplified and illuminating expression for the electric field of a normally-chirped 50 % duty-cycle pulse train (up to a constant overall phase shift relative to the expressions above) is:

$$E = E_o \cos\left(\frac{\pi}{2} \sin^2 \frac{\omega_{rep}t}{2}\right) e^{i\omega_c t - i\delta_{PM} \cos \omega_{rep} t}. \quad (4.4)$$

This can be understood as the product of a time-varying real amplitude  $a(t) = E_o \cos\left(\frac{\pi}{2} \sin^2 \frac{\omega_{rep}t}{2}\right)$

<sup>1</sup> This assumes that the modulation is applied to both paths in the intensity modulator with opposite sign; the correct ratios for a Mach-Zehnder intensity modulator with modulation in only one path are  $\eta_1 = -5.8$  dB and  $\eta_2 = -12.9$  dB. This difference arises from residual phase modulation on the output field in the latter case. To determine the internal configuration of the modulator, one can examine the action of the bias: if the modulation is applied to both paths with opposite signs, the bias will adjust only the ratios between the odd- and even-order sidebands while leaving the ratios within each group fixed. However, if the modulation is applied to only one path, the bias will change the ratio of each sideband to the carrier. These conclusions are reached by application of various forms of the Jacobi-Anger expansion.

and a phase factor from which the instantaneous carrier frequency  $\omega(t) = \omega_c + \omega_{rep}\delta_{PM} \sin \omega_{rep}t$  can be calculated. The carrier frequency  $\omega(t)$  is increasing when the amplitude  $a(t)$  is at its maximum, corresponding to normal chirp on the pulses. Fig. 4.1 depicts the intensity  $|E|^2$  and instantaneous carrier frequency of the field given by Eq. 4.4, as well as the intensity profile corresponding to compression of the same spectrum to its transform limit.

#### 4.2 Generation of an EOM comb and detection of its carrier-envelope offset frequency

Here I describe the generation of an EOM comb with 10 GHz repetition rate and subsequent measurement of its carrier-envelope offset frequency. One advantage of the EOM comb scheme is that the generation and spectral broadening of the comb is well understood, and can be modeled accurately. To demonstrate this, I compare the results of simulations of the comb to the experimental output at each stage in the generation process.

The experimental setup is depicted in Fig. 4.2. The basic experimental scheme consists of the following steps: 1. Initial generation and temporal compression of the EOM comb pulse train; 2. Modest spectral broadening and temporal re-compression, along with propagation through a Fabry-Perot filter cavity for noise reduction (see Sec. 4.3); and 3. Octave-spanning supercontinuum generation and detection of the carrier-envelope offset frequency. The results described below represent the first time a frequency comb of this kind has been self-referenced. Key to the success of this approach is the implementation of nonlinear spectral broadening in two stages, which allows the second stage to be seeded with  $\sim 130$  fs pulses for coherent supercontinuum generation. Noise reduction with the Fabry-Perot filter cavity is also critical for coherent spectral broadening; I describe a characterization of this step below.

To generate the initial train of chirped pulses, a telecommunications-band CW laser is passed through cascaded phase and intensity modulators driven with a 10 GHz microwave signal. The intensity modulator is biased at the 50 % transmission point and driven with an RF amplitude appropriate for generation of a 50 % duty-cycle pulse train, as described above; the phase modulator is driven with modulation depth of  $\sim 31\pi/4 \sim 24.3$  rad. The relative phase between the modulators is set such that the phase applied by the phase modulator is at a minimum when the transmission of the intensity modulator is highest; this yields a train of normally-chirped (up-chirped) pulses. Fig. 4.2, Panel (i) presents a comparison between the simulated and measured spectra for the initial pulse train.

Next, the chirped pulse train is propagated through 600 m of anomalously-dispersive SMF. The length of SMF that is appropriate for pulse compression depends on the bandwidth of the optical pulses to be compressed; equivalently, it depends on both the phase-modulation depth and the repetition rate of the pulse train. This temporal compression reduces the duration of the optical pulses from  $\sim 50$  ps to  $\sim 1.5$  ps. A simulation of the resulting intensity profile and a comparison to the spectrum's transform-limited pulse profile is presented in Fig. 4.2, Panel (ii).

The compressed pulses are amplified to 400 mW average power in an erbium-doped fiber amplifier and launched into 100 m of HNLF. This section of HNLF has chromatic dispersion that is small and normal; this is carefully chosen to chirp the pulses via self-phase modulation while avoiding soliton-fission dynamics [87]. The result is a train of chirped  $\sim 1.5$  ps pulses exiting the fiber. In Fig. 4.3a we present the measured optical spectrum of this pulse train, as well as results of a numerical simulation of the spectral broadening in the 100 m of normally-dispersive HNLF. These simulations are conducted using the nonlinear Schrodinger equation (NLSE) including third order dispersion [17], taking as initial conditions the calculated SMF-compressed intensity profile of the EOM comb pulses shown in Fig. 4.2(ii). The dispersion values for the HNLF used in the simulation are  $D = -0.04$  ps/nm·km and  $D' = 0.003$  ps/nm<sup>2</sup>·km, close to the values specified by the manufacturer. The simulation method is described in detail in Appendix ??.

After propagation through the first section of HNLF, the pulses are passed through a high-finesse Fabry-Perot cavity for suppression of optical frequency fluctuations as discussed below. Then the pulses are temporally compressed again, this time using a commercial spatial light modulator

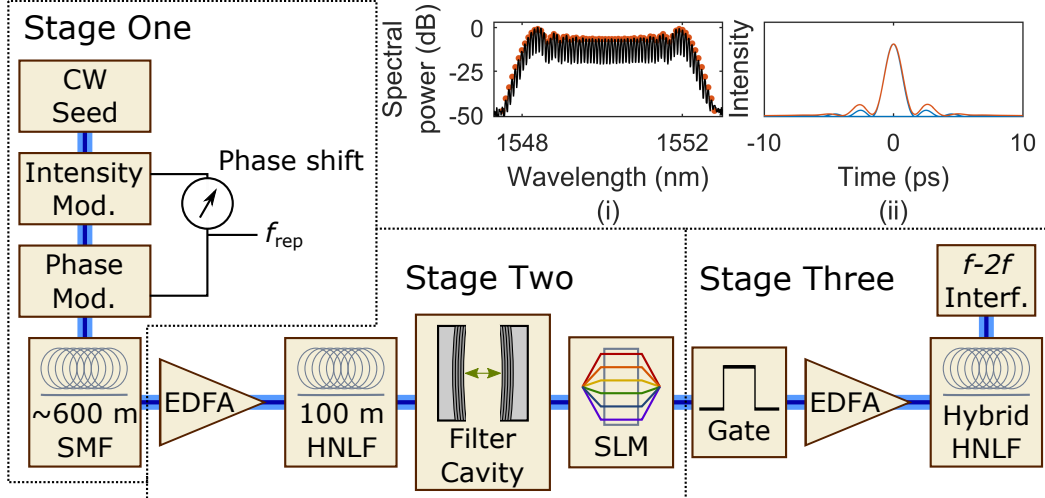


Figure 4.2: **Experimental setup for detection of the carrier-envelope offset frequency of an EOM comb after generation of a coherent supercontinuum.** Detection of  $f_0$  is performed with a three stage experiment. In Stage 1 a train of  $\sim 1.5$  ps pulses is generated. In Stage 2 these pulses are spectrally broadened and temporally compressed to  $\sim 130$  fs duration. In Stage 3 an octave-spanning supercontinuum is generated and  $f_0$  is detected in an  $f - 2f$  interferometer. Panel (i) shows the measured spectrum of the comb output by Stage 1 (black), along with a simulation of the same (orange). Panel (ii) shows simulation of the temporal compression of the pulses by propagation in 570 m of single-mode fiber (orange) and to the transform limit (blue).

(SLM) [88]; the SLM separates narrow spectral regions using a grating and passes them through individually controlled delaying elements before recombination. The SLM applies 2<sup>nd</sup>, 3<sup>rd</sup>, and 4<sup>th</sup> order chromatic dispersion, which simulations indicate is sufficient to compress the chirped pulses to  $\sim 130$  fs, near their transform limit. This is shown in Fig. 4.3b. While it is convenient, the SLM is not strictly necessary; it would also be possible to compress the pulses via propagation in an appropriate length of SMF. Figs. 4.3b and c present the compressed intensity profile and the evolution of the intensity profile, respectively, in simulated compression in SMF. Because the pulses are broadband, temporally short, and reasonably high energy, these simulations include the full dispersion profile of SMF and the Kerr nonlinearity.

The temporally compressed  $\sim 130$  fs pulses are then passed through an intensity modulator functioning as an electro-optic gate for repetition-rate downsampling (see Chapter ??). The gate selectively transmits every fourth pulse, reducing the repetition rate of the pulse train to 2.5 GHz. This facilitates coherent supercontinuum generation in a second stage of spectral broadening by increasing the pulse energy that can be achieved at a given average power. This step is convenient but not strictly necessary, as shown in Fig. ??.

The downsampled 2.5 GHz pulse train is amplified to an average power of 1.4 W, resulting in a train of  $\sim 0.56$  nJ pulses. This pulse train is propagated through 8 m of hybrid HNLF, yielding the spectrum shown in Fig. 4.3d. This hybrid HNLF consists of two segments with different dispersion profiles, with each segment serving a different purpose. The first segment is 30 cm long and highly dispersive<sup>2</sup> ( $D = 6$  ps/nm·km), and generates a dispersive wave centered at 1090 nm. The second segment is 7.7 m long and has lower dispersion ( $D = 1.5$  ps/nm·km), and generates a Raman-self-frequency-shifted soliton centered near 2000 nm. For this final stage of broadening it is difficult to achieve quantitative agreement between the measured supercontinuum spectrum and simulations

<sup>2</sup> We quantify the dispersion using the standard  $D$  parameter:  $D = -\frac{2\pi c}{\lambda^2} k''$ , where  $k''$  is the GVD parameter described in Chapter 1.

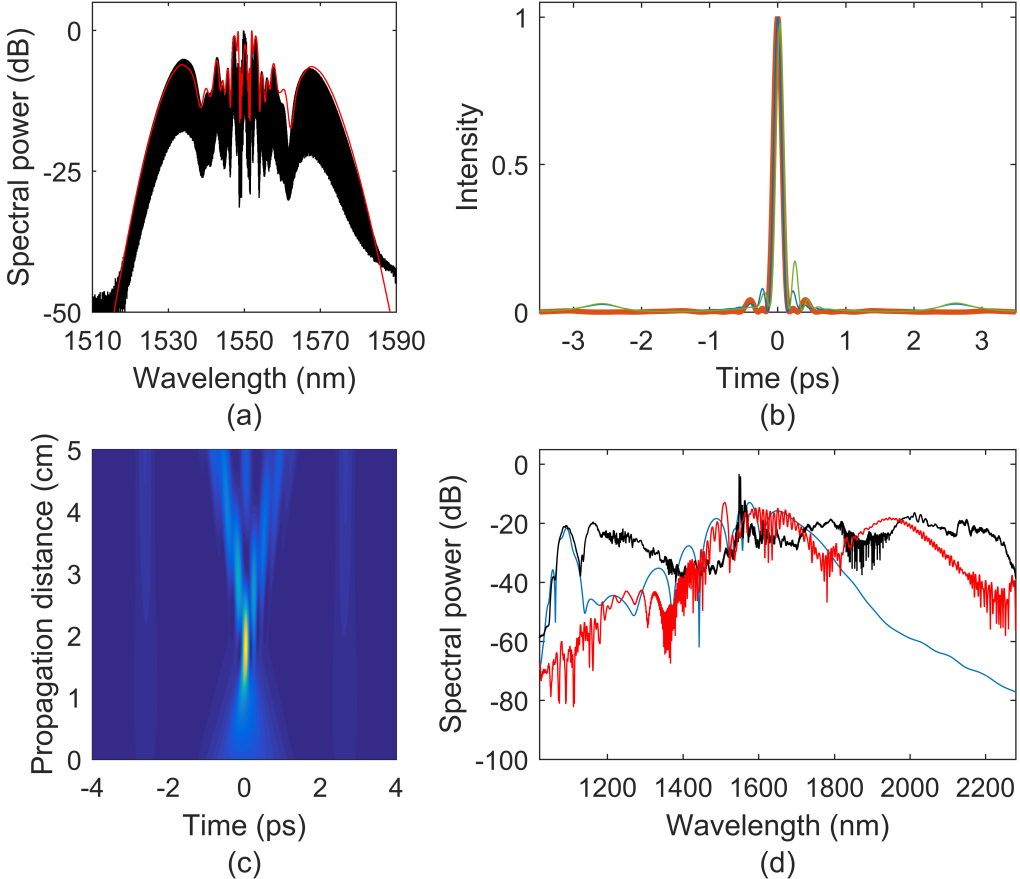


**Figure 4.3: Spectral broadening for generation of an octave-spanning supercontinuum.** (a) Measured optical spectrum after propagation in 100 m of low-normal-dispersion HNLF (black). The spectrum is broadened by self-phase modulation, which imposes a chirp on the pulses. Shown in red is a simulation of the same, conducted as described in the text. (b) Simulated pulse envelopes after temporal re-compression to the transform limit (thick orange), in the SLM with 2<sup>nd</sup>-, 3<sup>rd</sup>-, and 4<sup>th</sup>-order dispersion (blue), and in an appropriate length of SMF (green). FWHM pulse durations are similar, but the SLM- and SMF-compressed pulses have energy in satellite pulses at  $\pm 2.5$  s, and the SMF-compressed pulse has a significant asymmetry. (c) False-color plot of simulated re-compression of the SPM-chirped pulses (red spectrum in panel (a)) in SMF. A minimum pulse duration of  $\sim 140$  fs is achieved after propagating through 1.93 cm of SMF. (d) Measured optical spectrum of the octave-spanning supercontinuum generated by the EOM comb system (black), plotted along with simulated spectra calculated as described in the text to investigate the effects of the 30 cm, highly-dispersive piece of HNLF (blue) and the 7.7 m, lower-dispersion piece of HNLF (red).

due to the sensitivity of the higher-order nonlinear effects (e.g. Raman and self-steepening) on the input parameters. However, the qualitative effect of each of the fibers that make up the hybrid HNLF can be understood by modeling propagation in each section separately. To do this we use the LaserFOAM program [89], which employs the generalized NLS equation including Raman scattering, self-steepening, and 2<sup>nd</sup>- through 4<sup>th</sup>-order dispersion. The simulations are run independently, and both take as their initial conditions 170 fs sech pulses with 350 pJ energy, close to the energy coupled into the HNLF after accounting for losses. The results of these simulations are plotted in Fig. 4.3d.

The supercontinuum generated in the hybrid HNLF is coherent and suitable for  $f - 2f$  self-referencing. To detect the carrier-envelope offset frequency of the EOM comb, we pass the pulse train through an interferometer (see Fig. ??) consisting of a dichroic mirror, a delay stage in one path, and a 10 mm sample of periodically-poled lithium niobate that generates the second harmonic of supercontinuum light at 2140 nm. The dichroic mirror and delay stage enable adjustment of the relative timing between the native 1070 nm and doubled 2140 nm components of the supercontinuum so that they are temporally coincident. An optical band-pass filter centered at 1070 nm selects the supercontinuum components required for self-referencing, shown in Fig. 4.4a, and impinging the filtered light on a photodetector reveals the carrier-envelope offset frequency of the EOM comb, shown in Fig. 4.3b. Note that downsampling introduces an ambiguity in the offset frequency due to the increased density of comb modes in the downsampled pulse train; this ambiguity can be removed by measuring the change in measured offset frequency with a change in  $f_{rep} = \omega_{rep}/2\pi$  provided by the synthesizer driving the modulators.

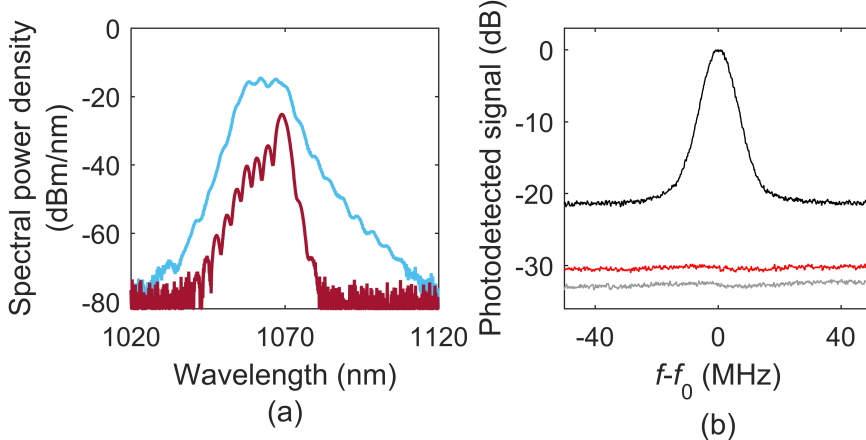
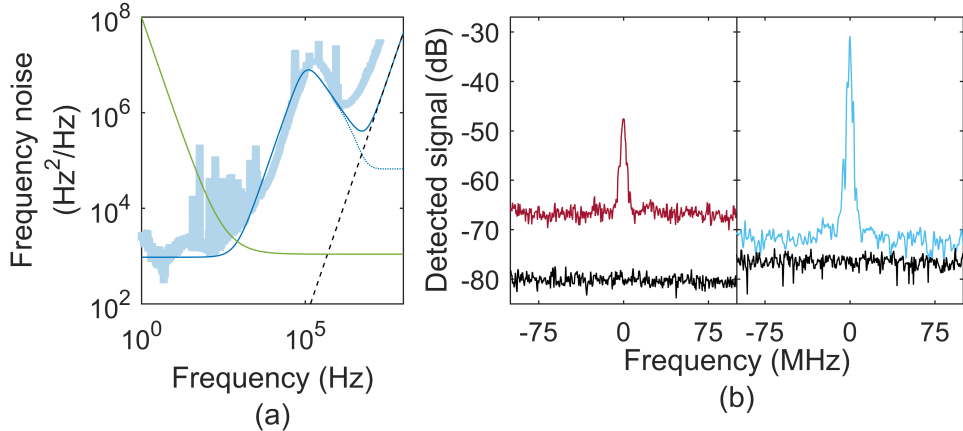


Figure 4.4: **Self-referencing of an EOM comb.** (a) Spectral components used for  $f - 2f$  self-referencing after passing through a 1070-nm optical bandpass filter: native supercontinuum light (blue) and frequency-doubled 2140-nm supercontinuum light (red). (b) Photodetected carrier-envelope offset frequency signal (black), along with a measurement of the intensity noise of the pulse train and the photodetector noise floor (grey). The frequency of the detected signal is  $f_0 = 706.6$  MHz.

### 4.3 Noise considerations in EOM comb generation

The repetition rate of an EOM comb is derived from a microwave source and is multiplied directly by a factor  $\mu$  to yield the frequency-comb mode with seed-laser-referenced mode number  $\mu$ . This is an important contrast with both modelocked-laser-based combs and microcombs, where generation of the comb in a resonant cavity dampens fast fluctuations of  $f_{rep}$ . In the EOM comb case, the contribution to the frequency noise of mode  $\mu$  from the microwave source scales with  $\mu$ ; the contribution to the power spectrum of frequency noise scales as  $\mu^2$ . This presents a challenge in the generation of the coherent octave-spanning supercontinuum spectrum required for  $f - 2f$  self-referencing, as the modes used for self-referencing are at the extreme ends of the supercontinuum where  $\mu$  is large. The factor by which the noise on the modulation tone  $f_{rep}$  is multiplied to determine its contribution to the noise on the measured carrier-envelope offset frequency is the ratio between the frequency  $f_c$  of the seed laser and the repetition rate. It is easiest to see this by recalling that the carrier-envelope offset frequency, which is measured by  $f - 2f$  self-referencing, is  $f_0 = f_c - Nf_{rep}$ , where  $N$  is the largest integer such that  $f_0 > 0$ ; therefore  $\partial f_0 / \partial f_{rep} = -N$ .

For the 10 GHz comb discussed above the noise on  $f_{rep}$  contributes to the noise on  $f_0$  after multiplication by a factor  $N = f_c/f_{rep} \sim 19340$  (where  $f_c = 193.4$  THz for a 1550 nm seed laser). In Fig. 4.5a we plot this contribution to the spectrum of fluctuations the carrier-envelope offset frequency, as well as the contribution from the noise of the seed laser. The noise on  $f_{rep}$  results from technical noise on the synthesizer tone at low Fourier frequencies and approaches a white Johnson-Nyquist (thermal) phase-noise floor of -177 dBm/Hz at high Fourier frequencies. Noise in each of these regimes impacts the photodetected  $f_0$  signal: low-frequency noise contributes to the linewidth of the comb modes and therefore the  $f_0$  signal, while high-frequency noise contributes to a frequency-noise floor on the photodetected signal [90]. Unmitigated multiplication of this thermal floor by the factor  $N^2 = 19340^2$  leads to a supercontinuum with optical frequency fluctuations that are large enough to prevent detection and measurement of  $f_0$ ; this is evidenced by unsuccessful attempts we have made to measure  $f_0$  without the filter cavity in place.



**Figure 4.5: Investigation of the noise properties of the EOM comb.** (a) Contributions to the frequency-noise spectrum of the carrier-envelope offset frequency: model of the seed laser based on past measurements (green), model of the 10 GHz synthesizer multiplied by  $19340^2$  without the filter cavity (solid blue, measurement thick blue), and synthesizer multiplied by  $19340^2$  and the Lorentzian filter-cavity transfer function (dotted blue). The synthesizer is modeled at high frequency by noise increasing as  $f^2$  (associated with a white phase-noise floor) that arises from Johnson-Nyquist noise with synthesizer power of -8 dBm. The thermal contribution alone is indicated by the dashed black line. (b) Comparison of the detected beats between the supercontinuum and a CW laser with 1319 nm wavelength without (red, left) and with (blue, right) the Fabry-Perot filter cavity. The level of intensity noise on the supercontinuum, measured by removing the 1319 nm CW laser, is shown by the lower gray trace in each plot; the elevated floor of the red trace relative to this background indicates that frequency noise is responsible for the reduced SNR of the beat without the filter cavity. Signal-to-noise ratios for the beat are 17 dB without and 40 dB with the filter cavity.

Inclusion of the Fabry-Perot filter cavity in our system enables detection and measurement of  $f_0$ . We use a Fabry-Perot cavity with free-spectral range  $\sim 10$  GHz that is actively stabilized to the comb's mode spacing. Our filter cavity has linewidth 7.5 MHz; equivalently, it has finesse of  $\mathcal{F}=1333$ . The filter cavity's Lorentzian transfer function reduces the optical frequency fluctuations of the comb modes at high Fourier frequency—these fluctuations are averaged over the photon lifetime of the cavity. The effect of passing the comb through the cavity is demonstrated concretely in Fig. 4.5b, where we compare the lineshape of a heterodyne beat between the supercontinuum and a CW laser with 1319 nm wavelength with and without the filter cavity in place. The signal-to-noise ratios for the beat with and without the filter cavity are 40 dB and 17 dB, respectively.

The filter cavity reduces the frequency noise of  $f_0$  at Fourier frequencies outside of the cavity

linewidth of 7.5 MHz. We explore the effect of fluctuations inside of the filter cavity's linewidth by changing the microwave source from which  $f_{rep}$  is derived. The  $f_0$  signal shown in Fig. 4.4b is acquired with a tunable commercial synthesizer providing  $f_{rep}$  after repetition-rate downsampling to 2.5 GHz. In Fig. 4.6 we show the detected  $f_0$  signal with three different sources for the 10 GHz repetition rate: 1. No downsampling, synthesizer at 10 GHz; 2. Dielectric-resonator oscillator; and 3. Sapphire oscillator. The  $f_0$  beat without downsampling with  $f_{rep}$  derived from the synthesizer has signal-to-noise ratio comparable to that of the  $f_0$  beat measured at 2.5 GHz repetition rate, but with higher intensity noise on the supercontinuum due to uncontrolled differences in the nonlinear spectral broadening. The other two sources have significantly less noise at low Fourier frequencies, and the effect of this lower noise is readily apparent in the reduced linewidth of the  $f_0$  signal. This indicates the importance of a high-performance microwave oscillator for future deployments of EOM combs. We emphasize that we have been unable to detect  $f_0$  without the filter cavity, even with  $f_{rep}$  derived from the sapphire oscillator. This is a confirmation that oscillator-independent thermal noise obscures  $f_0$  without the filter cavity in place.

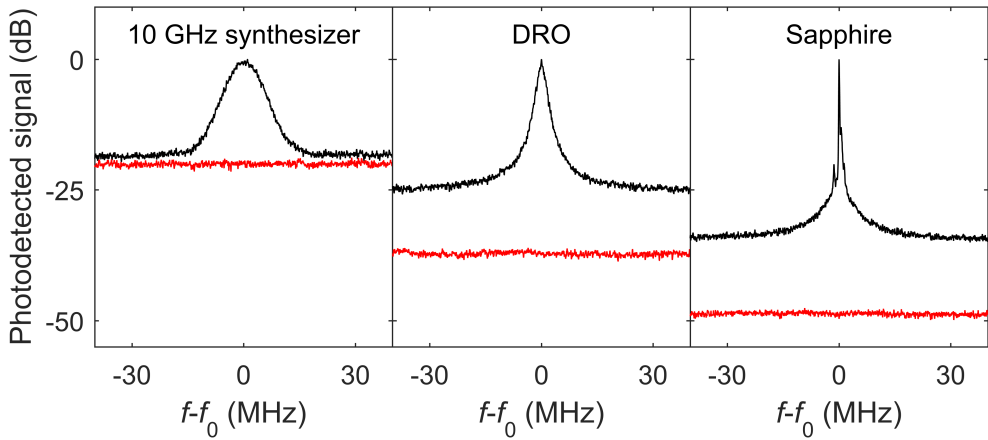


**Figure 4.6: Photodetected carrier-envelope-offset frequency signal with different sources for  $f_{rep}$ .** (a) The  $f_0$  beat with  $f_{rep}$  derived from a synthesizer;  $f_0 = 1.793$  GHz. (b) The same, with  $f_{rep}$  derived from a dielectric-resonator oscillator;  $f_0 = 491$  MHz. (c) The same, with  $f_{rep}$  derived from a sapphire oscillator,  $f_0 = 726$  MHz. Different  $f_0$  linewidths for different  $f_{rep}$  sources illustrate the effect of low-Fourier-frequency noise of  $f_{rep}$  on the frequency-noise characteristics of the EOM comb.

#### 4.4 Application: Optical frequency division via double pinning

*Optical frequency division* (OFD) refers to the stabilization of a microwave frequency by locking it to a subharmonic of an optical frequency or frequency difference [91, 92]. This technique transfers the fractional frequency stability of the optical frequency to the microwave tone, and is a method for generation of stable microwaves that is competitive with all-electronic techniques. One method for OFD is to self-reference a frequency comb and lock  $f_0$  to a microwave reference, and then lock the beat between the comb and a stable optical frequency  $\nu_{opt}$  by feeding back to the repetition rate. An ideal lock transfers the noise on  $\nu_{opt}$  to the repetition rate with a division factor  $N$ , where the beat is taken between  $\nu_{opt}$  and mode  $N$  with frequency  $f_0 + Nf_{rep}$ . The repetition rate then acquires the fractional frequency stability of the optical reference.

A second method of performing OFD is *double pinning*, in which the comb is not self-referenced, but instead two optical references are used to control the two comb degrees of freedom  $f_{rep}$  and  $f_0$  [69, 93, 94]. As a demonstration of the utility of the EOM comb system, we perform OFD with

double pinning using the EOM comb spectrum generated as described above.

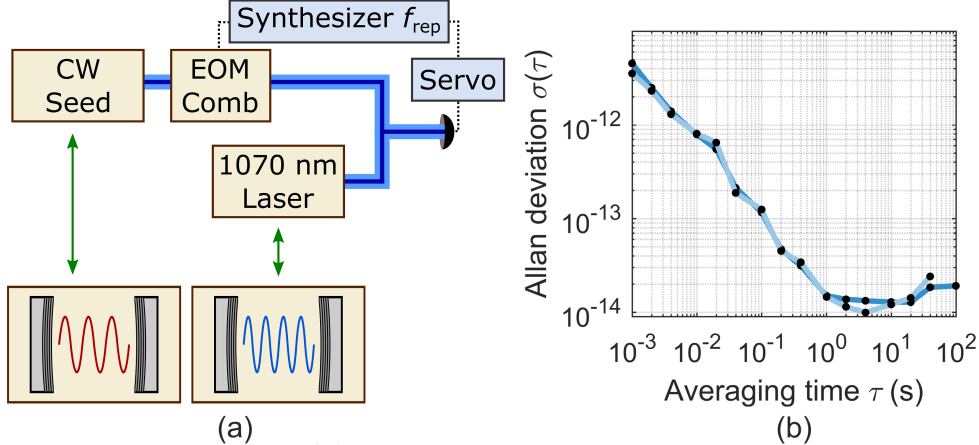


Figure 4.7: **Stable microwave generation with an EOM comb via double pinning.** (a) Experimental setup for double pinning of an EOM comb to two optical references. The seed laser for the EOM comb is locked to a stable reference cavity at 1550 nm, and a mode of the supercontinuum is locked to a second laser stabilized to a reference cavity at 1070 nm. The lock is achieved by feeding back to the synthesizer that generates  $f_{rep}$ . (b) Measurement of the Allan deviation of the repetition rate of the double-pinned EOM comb. The Allan deviation at 1 s averaging time is  $\sim 1.3 \times 10^{-14}$ , considerably better than what can be achieved by the synthesizer alone. At longer averaging times the frequency interval  $f_{1070} - f_{1550}$  begins to change due to thermal drift, so the Allan deviation increases.

For our OFD experiment, we generate the EOM comb using a seed laser with frequency  $f_{1550}$  that is locked to a stable reference cavity for 1550 nm wavelength. We also generate a second laser with frequency  $f_{1070}$  that is stabilized to a reference cavity for 1070 nm wavelength. After generating the EOM comb supercontinuum, we measure the frequency of the beat between a mode of the EOM comb with pump-referenced mode number  $\mu_b$  and frequency  $f_{\mu b} = f_{1550} + \mu_b f_{rep}$  and the cavity-stabilized 1070 nm laser. We lock this beat to a microwave reference with frequency  $f_{lock}$  by feeding back to the repetition rate of the EOM comb. This experimental setup is depicted schematically in Fig. 4.7a. The equation representing an ideal lock is:

$$0 = f_{1550} + \mu_b f_{rep} - f_{1070} - f_{lock}. \quad (4.5)$$

Then the fluctuations on the repetition rate are:

$$\delta f_{rep} = \delta(f_{1070} - f_{1550} + f_{lock})/\mu_b. \quad (4.6)$$

Thus, the fluctuations on the repetition rate are the worse of (a) the absolute fluctuations on  $f_b$  divided by  $\mu_b$  and (b) the fractional fluctuations on  $f_{1070} - f_{1550}$ , since  $f_{1070} - f_{1550} \sim \mu_b f_{rep}$ .

We characterize the output of this OFD scheme by photodetecting the repetition rate of the OFD-stabilized EOM comb and measuring its Allan deviation  $\sigma(\tau)$  [95]. The Allan deviation is the square root of the Allan variance  $\sigma^2(\tau)$ , which is defined as:

$$\sigma^2(\tau) = \frac{1}{2} < (\bar{y}_{n+1} - \bar{y}_n)^2 >. \quad (4.7)$$

Here  $< g >$  denotes the expectation value of  $g$ , which in practice is determined by recording many samples, and  $\bar{y}_n$  is the  $n^{\text{th}}$  fractional frequency average, where each average is over a time  $\tau$  and

there is no dead time between them. The fractional frequency  $y$  is defined relative to a nominal frequency  $f_{nom}$ :  $y(t) = (f(t) - f_{nom})/f_{nom}$ .

We measure the Allan deviation of  $f_{rep}$  by measuring the difference between  $f_{rep}$  and a reference 10 GHz signal that is derived through OFD with a Ti:sapphire modelocked laser [92]; the reference is known to have Allan deviation significantly lower than what we measure, so we know that the observed Allan deviation is not limited by the noise-floor of the measurement. We plot the results of the measurement,  $\sigma(\tau)$  as a function of averaging time  $\tau$ , for two separate measurements in Fig. 4.7b. The observed Allan deviation at one second averaging time  $\sigma(\tau = 1 \text{ s}) \sim 1.3 \times 10^{-14}$  is significantly better than the level  $\sim 10^{-13}$  that is achieved by the synthesizer alone, using just the hydrogen maser at NIST as a reference.

## 4.5 Outlook

The EOM comb approach for frequency-comb generation yields combs that are widely tunable and that can be flexibly tailored for specific applications. Because the comb generation is a non-resonant process (up to the optional inclusion of a filter cavity), the comb properties can be manipulated in real time with speed and range that greatly exceeds the capabilities of mode-locked lasers (where repetition-rate adjustment requires manipulation of moving parts) and microcombs (where repetition-rate control via phase modulation as described in Chap. ??, for example, is limited to the locking range afforded by the resonator dispersion). This has allowed, for example, the proposal and demonstration of ‘PHIRE’—Parallel Heterodyne Interferometry via Rep-rate Exchange—which is, essentially, dual-comb spectroscopy [96] with a single frequency comb whose repetition-rate is periodically switched [97].

EOM combs, with their lack of moving parts, also offer robust turn-key operation to a degree that is difficult to achieve with other comb sources. This has made them particularly promising for applications where long-term deployment with maximum up-time is important, such as calibration of astronomical spectrograms [98]. While the necessity of the filter cavity described here to enable  $f - 2f$  self-referencing is an apparent limitation, there are promising routes towards eliminating this requirement—using a high-power, tunable microwave oscillator could allow self-referencing of a repetition-rate-tunable EOM comb without a filter cavity.

## References

- [1] P Del'Haye, A Schliesser, O Arcizet, T Wilken, R Holzwarth, and T J Kippenberg. Optical frequency comb generation from a monolithic microresonator. *Nature*, 450 (7173), **2007**, 1214–1217 (cited on pages 1, 7).
- [2] T J Kippenberg, R Holzwarth, and S A Diddams. Microresonator-Based Optical Frequency Combs. *Science (New York, N.Y.)*, 332 (6029), **2011**, 555–559 (cited on pages 1, 6).
- [3] A A Savchenkov, A B Matsko, and L Maleki. On Frequency Combs in Monolithic Resonators. *Nanophotonics*, 5, **2016**, 363–391 (cited on page 1).
- [4] Yanne K. Chembo. Kerr optical frequency combs: Theory, applications and perspectives. *Nanophotonics*, 5 (2), **2016**, 214–230 (cited on page 1).
- [5] Alessia Pasquazi, Marco Peccianti, Luca Razzari, David J. Moss, Stéphane Coen, Miro Erkintalo, Yanne K. Chembo, Tobias Hansson, Stefan Wabnitz, Pascal Del'Haye, Xiaoxiao Xue, Andrew M. Weiner, and Roberto Morandotti. Micro-combs: A novel generation of optical sources. *Physics Reports*, 729, **2017**, 1–81 (cited on page 1).
- [6] Hansuek Lee, Tong Chen, Jiang Li, Ki Youl Yang, Seokmin Jeon, Oskar Painter, and Kerry J. Vahala. Chemically etched ultrahigh-Q wedge-resonator on a silicon chip. *Nature Photonics*, 6 (6), **2012**, 369–373. arXiv: 1112.2196 (cited on pages 1, 2).
- [7] Xu Yi, Qi-Fan Yang, Ki Youl Yang, Myoung-Gyun Suh, and Kerry Vahala. Soliton frequency comb at microwave rates in a high-Q silica microresonator. *Optica*, 2 (12), **2015**, 1078–1085 (cited on pages 1, 17).
- [8] Pascal Del'Haye, Scott A. Diddams, and Scott B. Papp. Laser-machined ultra-high-Q microrod resonators for nonlinear optics. *Applied Physics Letters*, 102, **2013**, 221119 (cited on pages 1, 3).
- [9] W Liang, A A Savchenkov, A B Matsko, V S Ilchenko, D Seidel, and L Maleki. Generation of near-infrared frequency combs from a MgF<sub>2</sub> whispering gallery mode resonator. *Optics Letters*, 36 (12), **2011**, 2290–2292 (cited on page 1).
- [10] Anatoliy a. Savchenkov, Andrey B. Matsko, Vladimir S. Ilchenko, Iouri Solomatine, David Seidel, and Lute Maleki. Tunable optical frequency comb with a crystalline whispering gallery mode resonator. *Physical Review Letters*, 101 (9), **2008**, 1–4. arXiv: 0804.0263 (cited on page 1).
- [11] Yoshitomo Okawachi, Kasturi Saha, Jacob S. Levy, Y. Henry Wen, Michal Lipson, and Alexander L. Gaeta. Octave-spanning frequency comb generation in a silicon nitride chip. *Optics Letters*, 36 (17), **2011**, 3398–3400. arXiv: 1107.5555 (cited on page 1).
- [12] D J Moss, R Morandotti, A L Gaeta, and M Lipson. New CMOS-compatible platforms based on silicon nitride and Hydex for nonlinear optics. *Nature Photonics*, 7 (July), **2013**, 597–607 (cited on page 1).
- [13] Danielle Braje, Leo Hollberg, and Scott Diddams. Brillouin-Enhanced Hyperparametric Generation of an Optical Frequency Comb in a Monolithic Highly Nonlinear Fiber Cavity Pumped by a cw Laser. *Physical Review Letters*, 102 (19), **2009**, 193902 (cited on pages 1, 18, 27).

- [14] Ewelina Obrzud, Steve Lecomte, and Tobias Herr. Temporal solitons in microresonators driven by optical pulses. *Nature Photonics*, 11 (August), **2017**, 600–607. arXiv: 1612.08993 (cited on pages 1, 17, 18, 27).
- [15] Vladimir S. Ilchenko and Andrey B. Matsko. Optical resonators with whispering-gallery modes - Part II: Applications. *IEEE Journal on Selected Topics in Quantum Electronics*, 12 (1), **2006**, 15–32 (cited on page 1).
- [16] Ki Youl Yang, Katja Beha, Daniel C. Cole, Xu Yi, Pascal Del'Haye, Hansuek Lee, Jiang Li, Dong Yoon Oh, Scott A. Diddams, Scott B. Papp, and Kerry J. Vahala. Broadband dispersion-engineered microresonator on a chip. *Nature Photonics*, 10 (March), **2016**, 316–320 (cited on page 2).
- [17] Govind P. Agrawal. **Nonlinear Fiber Optics**. 4th. Burlington, MA: Elsevier, 2007 (cited on pages 2, 6–8, 13, 30).
- [18] Maria L Calvo and Vasudevan Lakshminarayanan, eds. **Optical Waveguides: From Theory to Applied Technologies**. Boca Raton, FL: Taylor & Francis, 2007 (cited on page 2).
- [19] A N Oraevsky. Whispering-gallery waves. *Quantum Electronics*, 32 (42), **2002**, 377–400. arXiv: arXiv:1011.1669v3 (cited on page 3).
- [20] Hermann A. Haus. **Waves and Fields in Optoelectronics**. Englewood Cliffs: Prentice-Hall, 1984 (cited on page 3).
- [21] J. C. Knight, G. Cheung, F. Jacques, and T. A. Birks. Phase-matched excitation of whispering-gallery-mode resonances by a fiber taper. *Optics Letters*, 22 (15), **1997**, 1129 (cited on page 4).
- [22] S. M. Spillane, T. J. Kippenberg, O. J. Painter, and K. J. Vahala. Ideality in a Fiber-Taper-Coupled Microresonator System for Application to Cavity Quantum Electrodynamics. *Physical review letters*, 91 (4), **2003**, 043902 (cited on page 4).
- [23] Ehsan Shah Hosseini, Siva Yegnanarayanan, Amir Hossein Atabaki, Mohammad Soltani, and Ali Adibi. Systematic design and fabrication of high-Q single-mode pulley-coupled planar silicon nitride microdisk resonators at visible wavelengths. *Optics Express*, 18 (3), **2010**, 2127 (cited on page 4).
- [24] Tal Carmon, Lan Yang, and Kerry J Vahala. Dynamical thermal behavior and thermal self-stability of microcavities. *Optics Express*, 12 (20), **2004**, 4742–4750 (cited on page 4).
- [25] Robert W. Boyd. **Nonlinear Optics**. San Diego, CA: Elsevier, 2003 (cited on page 6).
- [26] Raúl del Coso and Javier Solis. Relation between nonlinear refractive index and third-order susceptibility in absorbing media. *Journal of the Optical Society of America B*, 21 (3), **2004**, 640 (cited on page 6).
- [27] T. Kippenberg, S. Spillane, and K. Vahala. Kerr-Nonlinearity Optical Parametric Oscillation in an Ultrahigh-Q Toroid Microcavity. *Physical Review Letters*, 93 (8), **2004**, 083904 (cited on page 7).
- [28] Anatoliy A. Savchenkov, Andrey B. Matsko, Dmitry Strekalov, Makan Mohageg, Vladimir S. Ilchenko, and Lute Maleki. Low threshold optical oscillations in a whispering gallery mode CaF<sub>2</sub> resonator. *Physical Review Letters*, 93 (24), **2004**, 2–5 (cited on page 7).
- [29] Imad H. Agha, Yoshitomo Okawachi, Mark A. Foster, Jay E. Sharping, and Alexander L. Gaeta. Four-wave-mixing parametric oscillations in dispersion-compensated high- Q silica microspheres. *Physical Review A - Atomic, Molecular, and Optical Physics*, 76 (4), **2007**, 1–4 (cited on page 7).
- [30] T. Herr, V. Brasch, J. D. Jost, C. Y. Wang, N. M. Kondratiev, M. L. Gorodetsky, and T. J. Kippenberg. Temporal solitons in optical microresonators. *arXiv*, **2012**, 1211.0733. arXiv: 1211.0733 (cited on pages 7, 16).

- [31] T. Herr, V. Brasch, J. D. Jost, C. Y. Wang, N. M. Kondratiev, M. L. Gorodetsky, and T. J. Kippenberg. Temporal solitons in optical microresonators. *Nature Photonics*, 8 (2), **2014**, 145–152. arXiv: [1211.0733](https://arxiv.org/abs/1211.0733) (cited on pages 7, 8, 15, 16, 22).
- [32] François Leo, Stéphane Coen, Pascal Kockaert, Simon-Pierre Gorza, Philippe Emplit, and Marc Haelterman. Temporal cavity solitons in one-dimensional Kerr media as bits in an all-optical buffer. *Nature Photonics*, 4 (7), **2010**, 471–476 (cited on pages 7, 26).
- [33] T. Herr, K. Hartinger, J. Riemensberger, C. Y. Wang, E. Gavartin, R. Holzwarth, M. L. Gorodetsky, and T. J. Kippenberg. Universal formation dynamics and noise of Kerr-frequency combs in microresonators. *Nature Photonics*, 6 (7), **2012**, 480–487 (cited on page 7).
- [34] Yanne K. Chembo and Curtis R. Menyuk. Spatiotemporal Lugiato-Lefever formalism for Kerr-comb generation in whispering-gallery-mode resonators. *Physical Review A*, 87, **2013**, 053852 (cited on page 7).
- [35] Stéphane Coen, Hamish G Randle, Thibaut Sylvestre, and Miro Erkintalo. Modeling of octave-spanning Kerr frequency combs using a generalized mean-field Lugiato-Lefever model. *Optics letters*, 38 (1), **2013**, 37–39 (cited on pages 7–9).
- [36] M. Haelterman, S. Trillo, and S. Wabnitz. Dissipative modulation instability in a nonlinear dispersive ring cavity. *Optics Communications*, 91 (5-6), **1992**, 401–407 (cited on page 7).
- [37] T Hansson, M Bernard, and S Wabnitz. Modulational Instability of Nonlinear Polarization Mode Coupling in Microresonators. 35 (4), **2018**. arXiv: [arXiv : 1802 . 04535v1](https://arxiv.org/abs/1802.04535v1) (cited on page 8).
- [38] Y K Chembo, I S Grudinin, and N Yu. Spatiotemporal dynamics of Kerr-Raman optical frequency combs. *Physical Review A*, 92 (4), **2015**, 4 (cited on page 8).
- [39] Cyril Godey, Irina V. Balakireva, Aurélien Coillet, and Yanne K. Chembo. Stability analysis of the spatiotemporal Lugiato-Lefever model for Kerr optical frequency combs in the anomalous and normal dispersion regimes. *Physical Review A*, 89 (6), **2014**, 063814 (cited on pages 9, 10).
- [40] I. V. Barashenkov and Yu S. Smirnov. Existence and stability chart for the ac-driven, damped nonlinear Schrödinger solitons. *Physical Review E - Statistical Physics, Plasmas, Fluids, and Related Interdisciplinary Topics*, 54 (5), **1996**, 5707–5725 (cited on pages 9, 15).
- [41] A Coillet and Y K Chembo. Routes to spatiotemporal chaos in Kerr optical frequency combs. *Chaos*, 24 (1), **2014**, 5. arXiv: [arXiv:1401.0927v1](https://arxiv.org/abs/1401.0927v1) (cited on pages 11, 24).
- [42] L A Lugiato and R Lefever. Spatial Dissipative Structures in Passive Optical Systems. *Physical Review Letters*, 58 (21), **1987**, 2209–2211 (cited on page 12).
- [43] LA Lugiato and R Lefever. Diffraction stationary patterns in passive optical systems. *Interaction of Radiation with Matter*, **1987** (cited on page 12).
- [44] William H. Renninger and Peter T. Rakich. Closed-form solutions and scaling laws for Kerr frequency combs. *Scientific Reports*, 6 (1), **2016**, 24742. arXiv: [1412.4164](https://arxiv.org/abs/1412.4164) (cited on page 12).
- [45] John Scott Russell. Report on Waves. *Fourteenth meeting of the British Association for the Advancement of Science*, **1844**, 311–390 (cited on page 12).
- [46] M. Brambilla, L. A. Lugiato, F. Prati, L. Spinelli, and W. J. Firth. Spatial soliton pixels in semiconductor devices. *Physical Review Letters*, 79 (11), **1997**, 2042–2045 (cited on page 12).
- [47] S. Minardi, F. Eilenberger, Y. V. Kartashov, A. Szameit, U. Röpke, J. Kobelke, K. Schuster, H. Bartelt, S. Nolte, L. Torner, F. Lederer, A. Tünnermann, and T. Pertsch. Three-dimensional light bullets in arrays of waveguides. *Physical Review Letters*, 105 (26), **2010**, 1–4. arXiv: [1101.0734](https://arxiv.org/abs/1101.0734) (cited on page 12).
- [48] F. X. Kärtner, I. D. Jung, and U. Keller. Soliton mode-locking with saturable absorbers. *IEEE Journal on Selected Topics in Quantum Electronics*, 2 (3), **1996**, 540–556 (cited on page 12).

- [49] P. Grelu and N. Akhmediev. Dissipative solitons for mode-locked lasers. *Nature Photonics*, 6 (February), **2012**, 84–92 (cited on page 12).
- [50] L. F. Mollenauer and J. P. Gordon. **Solitons in Optical Fibers**. Academic Press, 2006, p. 296 (cited on page 13).
- [51] A. Hasegawa and Y. Kodama. **Solitons in Optical Communications**. Academic Press, 1995 (cited on page 13).
- [52] Hermann A. Haus and William S. Wong. Solitons in optical communications. *Reviews of Modern Physics*, 68 (2), **1996**, 423–444 (cited on page 13).
- [53] Stéphane Coen and Miro Erkintalo. Universal scaling laws of Kerr frequency combs. *Optics letters*, 38 (11), **2013**, 1790–1792. arXiv: [arXiv:1303.7078v1](https://arxiv.org/abs/1303.7078v1) (cited on page 15).
- [54] H. Guo, M. Karpov, E. Lucas, A. Kordts, M. H.P. Pfeiffer, V. Brasch, G. Lihachev, V. E. Lobanov, M. L. Gorodetsky, and T. J. Kippenberg. Universal dynamics and deterministic switching of dissipative Kerr solitons in optical microresonators. *Nature Physics*, 13 (1), **2017**, 94–102. arXiv: [1601.05036](https://arxiv.org/abs/1601.05036) (cited on pages 15, 17).
- [55] N. J. Zabusky and M. D. Kruskal. Interaction of "solitons" in a collisionless plasma and the recurrence of initial states. *Physical Review Letters*, 15 (6), **1965**, 240 (cited on page 15).
- [56] J P Gordon. Interaction forces among solitons in optical fibers. *Optics Letters*, 8 (11), **1983**, 596 (cited on page 15).
- [57] Boris A. Malomed. Bound solitons in the nonlinear Schrodinger-Ginzburg-Landau equation. *Physical Review A*, 44 (10), **1991**, 6954–6957 (cited on page 15).
- [58] J K Jang, M Erkintalo, S G Murdoch, and S Coen. Ultraweak long-range interactions of solitons observed over astronomical distances. *Nature Photonics*, 7 (8), **2013**, 657–663. arXiv: [arXiv:1305.6670v1](https://arxiv.org/abs/1305.6670v1) (cited on page 15).
- [59] Pedro Parra-Rivas, Damia Gomila, Pere Colet, and Lendert Gelens. Interaction of solitons and the formation of bound states in the generalized Lugiato-Lefever equation. *European Physical Journal D*, 71 (7), **2017**, 198. arXiv: [arXiv:1705.02619v1](https://arxiv.org/abs/1705.02619v1) (cited on page 15).
- [60] Yadong Wang, François Leo, Julien Fatome, Miro Erkintalo, Stuart G. Murdoch, and Stéphane Coen. Universal mechanism for the binding of temporal cavity solitons, **2017**, 1–10. arXiv: [1703.10604](https://arxiv.org/abs/1703.10604) (cited on page 15).
- [61] Victor Brasch, Tobias Herr, Michael Geiselmann, Grigoriy Lihachev, Martin H. P. Pfeiffer, Michael L. Gorodetsky, and Tobias J. Kippenberg. Photonic chip-based optical frequency comb using soliton Cherenkov radiation. *Science*, 351 (6271), **2016**, 357. arXiv: [1410.8598](https://arxiv.org/abs/1410.8598) (cited on pages 17, 18).
- [62] Jordan R Stone, Travis C Briles, Tara E Drake, Daryl T Spencer, David R Carlson, Scott A Diddams, and Scott B Papp. Thermal and Nonlinear Dissipative-Soliton Dynamics in Kerr Microresonator Frequency Combs. *arXiv*, **2017**, 1708.08405. arXiv: [1708 . 08405](https://arxiv.org/abs/1708.08405) (cited on page 17).
- [63] V. E. Lobanov, G. V. Lihachev, N. G. Pavlov, A. V. Cherenkov, T. J. Kippenberg, and M. L. Gorodetsky. Harmonization of chaos into a soliton in Kerr frequency combs. *Optics Express*, 24 (24), **2016**, 27382. arXiv: [1607.08222](https://arxiv.org/abs/1607.08222) (cited on page 17).
- [64] Chaitanya Joshi, Jae K. Jang, Kevin Luke, Xingchen Ji, Steven A. Miller, Alexander Klenner, Yoshitomo Okawachi, Michal Lipson, and Alexander L. Gaeta. Thermally controlled comb generation and soliton modelocking in microresonators. *Optics Letters*, 41 (11), **2016**, 2565–2568. arXiv: [1603.08017](https://arxiv.org/abs/1603.08017) (cited on page 17).
- [65] Weiqiang Wang, Zhizhou Lu, Wenfu Zhang, Sai T. Chu, Brent E. Little, Leiran Wang, Xiaoping Xie, Mulong Liu, Qinghua Yang, Lei Wang, Jianguo Zhao, Guoxi Wang, Qibing Sun, Yuanshan Liu, Yishan Wang, and Wei Zhao. Robust soliton crystals in a thermally controlled microresonator. *Optics Letters*, 43 (9), **2018**, 2002–2005 (cited on page 17).

- [66] Jae K Jang, Miro Erkintalo, Stuart G Murdoch, and Stéphane Coen. Writing and erasing of temporal cavity solitons by direct phase modulation of the cavity driving field. *Optics Letters*, 40 (20), **2015**, 4755–4758. arXiv: 1501.05289 (cited on page 17).
- [67] Jae K Jang, Miro Erkintalo, Stephane Coen, and Stuart G Murdoch. Temporal tweezing of light through the trapping and manipulation of temporal cavity solitons. *Nature Communications*, 6, **2015**, 7370. arXiv: 1410.4836 (cited on page 17).
- [68] Yadong Wang, Bruno Garbin, Francois Leo, Stephane Coen, Miro Erkintalo, and Stuart G. Murdoch. Writing and Erasure of Temporal Cavity Solitons via Intensity Modulation of the Cavity Driving Field. *arXiv*, **2018**, 1802.07428. arXiv: 1802.07428 (cited on page 17).
- [69] Scott B. Papp, Katja Beha, Pascal Del'Haye, Franklyn Quinlan, Hansuek Lee, Kerry J. Vahala, and Scott A. Diddams. Microresonator frequency comb optical clock. *Optica*, 1 (1), **2014**, 10–14. arXiv: 1309.3525 (cited on pages 17, 35).
- [70] Myoung Gyun Suh, Qi Fan Yang, Ki Youl Yang, Xu Yi, and Kerry J. Vahala. Microresonator soliton dual-comb spectroscopy. *Science*, 354 (6312), **2016**, 1–5. arXiv: 1607.08222 (cited on page 17).
- [71] Pablo Marin-Palomo, Juned N. Kemal, Maxim Karpov, Arne Kordts, Joerg Pfeifle, Martin H.P. Pfeiffer, Philipp Trocha, Stefan Wolf, Victor Brasch, Miles H. Anderson, Ralf Rosenberger, Kovendhan Vijayan, Wolfgang Freude, Tobias J. Kippenberg, and Christian Koos. Microresonator-based solitons for massively parallel coherent optical communications. *Nature*, 546 (7657), **2017**, 274–279. arXiv: 1610.01484 (cited on page 17).
- [72] Daryl T Spencer, Tara Drake, Travis C Briles, Jordan Stone, Laura C Sinclair, Connor Fredrick, Qing Li, Daron Westly, B Robert Ilic, Aaron Bluestone, Nicolas Volet, Tin Komljenovic, Lin Chang, Seung Hoon Lee, Dong Yoon Oh, Tobias J Kippenberg, Erik Norberg, Luke Theogarajan, Myoung-gyun Suh, Ki Youl Yang, H P Martin, Kerry Vahala, Nathan R Newbury, Kartik Srinivasan, John E Bowers, Scott A Diddams, and Scott B Papp. An optical-frequency synthesizer using integrated photonics. *Nature*, 557, **2018**, 81–85 (cited on page 17).
- [73] J. D. Jost, T. Herr, C. Lecaplain, V. Brasch, M. H. P. Pfeiffer, and T. J. Kippenberg. Counting the cycles of light using a self-referenced optical microresonator. *Optica*, 2 (8), **2015**, 706–711. arXiv: 1411.1354 (cited on page 17).
- [74] Pascal Del'Haye, Aurélien Coillet, Tara Fortier, Katja Beha, Daniel C. Cole, Ki Youl Yang, Hansuek Lee, Kerry J. Vahala, Scott B. Papp, and Scott A. Diddams. Phase-coherent microwave-to-optical link with a self-referenced microcomb. *Nature Photonics*, 10 (June), **2016**, 1–5 (cited on page 17).
- [75] Victor Brasch, Erwan Lucas, John D. Jost, Michael Geiselmann, and Tobias J. Kippenberg. Self-referenced photonic chip soliton Kerr frequency comb. *Light: Science & Applications*, 6 (1), **2017**, e16202. arXiv: 1605.02801 (cited on page 17).
- [76] Travis C. Briles, Jordan R. Stone, Tara E. Drake, Daryl T. Spencer, Connor Frederick, Qing Li, Daron A. Westly, B. Robert Illic, Kartik Srinivasan, Scott A. Diddams, and Scott B. Papp. Kerr-microresonator solitons for accurate carrier-envelope-frequency stabilization. *arXiv*, **2017**, 1711.06251. arXiv: 1711.06251 (cited on page 17).
- [77] T. Kobayashi, T. Sueta, Y. Cho, and Y. Matsuo. High-repetition-rate optical pulse generator using a Fabry-Perot electro-optic modulator. *Applied Physics Letters*, 21 (8), **1972**, 341–343 (cited on page 28).
- [78] Motonobu Kourogi, Ken Nakagawa, and Motoichi Ohtsu. Wide-Span Optical Frequency Comb Generator for. 29 (10), **1993** (cited on page 28).
- [79] H. Murata, A. Morimoto, T. Kobayashi, and S. Yamamoto. Optical pulse generation by electrooptic-modulation method and its application to integrated ultrashort pulse generators. *IEEE Journal of Selected Topics in Quantum Electronics*, 6 (6), **2000**, 1325–1331 (cited on page 28).

- [80] Takahide Sakamoto, Tetsuya Kawanishi, and Masayuki Izutsu. Asymptotic formalism for ultraflat optical frequency comb generation using a Mach-Zehnder modulator. *Optics letters*, 32 (11), **2007**, 1515–1517 (cited on page 28).
- [81] Isao Morohashi, Takahide Sakamoto, Hideyuki Sotobayashi, Tetsuya Kawanishi, Iwao Hosako, and Masahiro Tsuchiya. Widely repetition-tunable 200 fs pulse source using a Mach-Zehnder-modulator-based flat comb generator and dispersion-flattened dispersion-decreasing fiber. *Optics letters*, 33 (11), **2008**, 1192–1194 (cited on page 28).
- [82] A. Ishizawa, T. Nishikawa, A. Mizutori, H. Takara, S. Aozasa, A. Mori, H. Nakano, A. Takada, and M. Koga. Octave-spanning frequency comb generated by 250 fs pulse train emitted from 25 GHz externally phase-modulated laser diode for carrier-envelope-offset-locking. *Electronics Letters*, 46 (19), **2010**, 1343 (cited on page 28).
- [83] Rui Wu, V. R. Supradeepa, Christopher M. Long, Daniel E. Leaird, and Andrew M. Weiner. Generation of very flat optical frequency combs from continuous-wave lasers using cascaded intensity and phase modulators driven by tailored radio frequency waveforms. *Optics Letters*, 35 (19), **2010**, 3234. arXiv: 1005.5373 (cited on page 28).
- [84] V. R. Supradeepa and Andrew M. Weiner. Bandwidth scaling and spectral flatness enhancement of optical frequency combs from phase-modulated continuous-wave lasers using cascaded four-wave mixing. *Optics Letters*, 37 (15), **2012**, 3066 (cited on page 28).
- [85] Andrew J Metcalf, Victor Torres-company, Daniel E Leaird, Senior Member, Andrew M Weiner, and Abstract Broadband. High-Power Broadly Tunable Electrooptic Frequency Comb Generator. *IEEE Journal of Selected Topics in Quantum Electronics*, 19 (6), **2013**, 3500306 (cited on page 28).
- [86] Rui Wu, Victor Torres-company, Daniel E Leaird, and Andrew M Weiner. Optical Frequency Comb Generation. 21 (5), **2013**, 6045–6052 (cited on page 28).
- [87] John M. Dudley, Goëry Goery Genty, and Stéphane Coen. Supercontinuum generation in photonic crystal fiber. *Reviews of Modern Physics*, 78 (4), **2006**, 1135–1184 (cited on page 30).
- [88] A. M. Weiner. Femtosecond pulse shaping using spatial light modulators. *Review of Scientific Instruments*, 71 (5), **2000**, 1929–1960 (cited on page 31).
- [89] a a Amorim, M V Tognetti, P Oliveira, J L Silva, L M Bernardo, F X Kärtner, and H M Crespo. Sub-two-cycle pulses by soliton self-compression in highly nonlinear photonic crystal fibers. *Optics letters*, 34 (24), **2009**, 3851–3853 (cited on page 32).
- [90] Gianni Di Domenico, Stéphane Schilt, and Pierre Thomann. Simple approach to the relation between laser frequency noise and laser line shape. *Applied optics*, 49 (25), **2010**, 4801–4807 (cited on page 34).
- [91] J. J. McFerran, E. N. Ivanov, A. Bartels, G. Wilpers, C. W. Oates, S. A. Diddams, and L. Hollberg. Low-noise synthesis of microwave signals from an optical source. *Electronics Letters*, 41 (11), **2005**, 650–651. arXiv: 0504102 [arXiv:physics] (cited on page 35).
- [92] T. M. Fortier, M. S. Kirchner, F. Quinlan, J. Taylor, J. C. Bergquist, T. Rosenband, N. Lemke, A. Ludlow, Y. Jiang, C. W. Oates, and S. A. Diddams. Generation of ultrastable microwaves via optical frequency division. *Nature Photonics*, 5 (7), **2011**, 425–429. arXiv: 1101.3616 (cited on pages 35, 37).
- [93] William C. Swann, Esther Baumann, Fabrizio R. Giorgetta, and Nathan R. Newbury. Microwave generation with low residual phase noise from a femtosecond fiber laser with an intracavity electro-optic modulator. *Optics Express*, 19 (24), **2011**, 24387. arXiv: arXiv: 1106.5195v1 (cited on page 35).
- [94] Jiang Li, Xu Yi, Hansuek Lee, Scott A Diddams, and Kerry J Vahala. Electro-optical frequency division and stable microwave synthesis. *Science*, 345 (6194), **2014**, 309–314 (cited on page 35).
- [95] Judah Levine. Introduction to time and frequency metrology. *Review of Scientific Instruments*, 70 (6), **1999**, 2567–2596 (cited on page 36).

- [96] Ian Coddington, Nathan Newbury, and William Swann. Dual-comb spectroscopy. *Optica*, 3 (4), **2016**, 414–426 (cited on page 37).
- [97] David R. Carlson, Daniel D. Hickstein, Daniel C. Cole, Scott A. Diddams, and Scott B. Papp. Dual-comb interferometry via repetition-rate switching of a single frequency comb. *arXiv*, **2018**, 1806.05311. arXiv: 1806.05311 (cited on page 37).
- [98] A. J. Metcalf, C. Bender, S. Blakeslee, W. Brand, D. Carlson, S. A. Diddams, C. Fredrick, S. Halverson, F. Hearty, D. Hickstein, J. Jennings, S. Kanodia, K. Kaplan, E. Lubar, S. Mahadevan, A. Monson, J. Ninan, C. Nitroy, S. Papp, L. Ramsey, P. Robertson, A. Roy, C. Schwab, K. Srinivasan, G. K. Stefansson, and R. Terrien. Infrared Astronomical Spectroscopy for Radial Velocity Measurements with 10 cm/s Precision. In: **Conference on Lasers and Electro-Optics**. 2018, JTh5A.1 (cited on page 37).